

# THE ICARUS EXPERIMENT, A Second-Generation Proton Decay Experiment and Neutrino Observatory at the Gran Sasso Laboratory

by the ICARUS Collaboration

F. Arneodo<sup>1</sup>, B. Babussinov<sup>2</sup>, A. Badertscher<sup>3</sup>, B. Badełek<sup>4</sup>, G. Battistoni<sup>5</sup>, P. Benetti<sup>6</sup>, E. Bernardini<sup>1</sup>, M. Bischofberger<sup>3</sup>, A. Borio di Tigliole<sup>7</sup>, R. Brunetti<sup>6</sup>, A. Bueno<sup>3</sup>, E. Calligarich<sup>6</sup>, M. Campanelli<sup>3</sup>, C. Carpanese<sup>3</sup>, D. Cavalli<sup>5</sup>, F. Cavanna<sup>8</sup>, P. Cennini<sup>9</sup>, S. Centro<sup>2</sup>, A. Cesana<sup>7</sup>, C. Chen<sup>10</sup>, Y. Chen<sup>10</sup>, D. Cline<sup>11</sup>, A. Dąbrowska<sup>12</sup>, R. Dolfini<sup>6</sup>, M. Felcini<sup>3</sup>, A. Ferrari<sup>9,†</sup>, K. He<sup>10</sup>, J. Holeczek<sup>13</sup>, X. Huang<sup>10</sup>, A. Gigli Berzolari<sup>6</sup>, I. Gil-Botella<sup>3</sup>, D. Grech<sup>14</sup>, B. Jokisz<sup>13</sup>, C. Juszczak<sup>14</sup>, J. Kisiel<sup>13</sup>, D. Kielczewska<sup>4</sup>, T. Kozłowski<sup>15</sup>, M. Laffranchi<sup>3</sup>, J. Lagoda<sup>4</sup>, Z. Li<sup>10</sup>, F. Lu<sup>10</sup>, J. Ma<sup>10</sup>, C. Matthey<sup>11</sup>, F. Mauri<sup>6</sup>, M. Markiewicz<sup>16</sup>, D. Mazza<sup>8</sup>, L. Mazzone<sup>6</sup>, G. Meng<sup>2</sup>, C. Montanari<sup>6</sup>, M. Moszyński<sup>15</sup>, S. Navas-Concha<sup>3</sup>, G. Nurzia<sup>8</sup>, S. Otwinowski<sup>11</sup>, O. Palamara<sup>1</sup>, D. Pascoli<sup>2</sup>, J. Pasternak<sup>14</sup>, L. Periale<sup>17</sup>, S. Petrera<sup>8</sup>, G. Piano Mortari<sup>8</sup>, A. Piazzoli<sup>6</sup>, P. Picchi<sup>17,‡</sup>, F. Pietropaolo<sup>9,§</sup>, A. Rappoldi<sup>6</sup>, G.L. Raselli<sup>6</sup>, J. Rico<sup>3</sup>, E. Rondio<sup>15</sup>, M. Rossella<sup>6</sup>, C. Rossi<sup>8</sup>, A. Rubbia<sup>3</sup>, C. Rubbia<sup>6,¶</sup>, P. Sala<sup>5</sup>, T. Rancati<sup>5</sup>, D. Scannicchio<sup>6</sup>, F. Sergiampietri<sup>18</sup>, J. Sobczyk<sup>14</sup>, N. Sinanis<sup>3</sup>, J. Stepaniak<sup>15</sup>, M. Stodulski<sup>12</sup>, M. Szeptycka<sup>15</sup>, M. Szleper<sup>15</sup>, M. Terrani<sup>7</sup>, S. Ventura<sup>2</sup>, C. Vignoli<sup>6</sup>, H. Wang<sup>11</sup>, M. Wójcik<sup>19</sup>, J. Woo<sup>11</sup>, G. Xu<sup>10</sup>, Z. Xu<sup>6</sup>, A. Zalewska<sup>12</sup>, J. Zalipska<sup>15</sup>, C. Zhang<sup>10</sup>, Q. Zhang<sup>10</sup>, S. Zhen<sup>10</sup>, W. Zipper<sup>13</sup>

<sup>1</sup>Laboratori Nazionali di Gran Sasso, INFN, s.s. 17bis, km 18+910, Assergi (AQ), Italy

<sup>2</sup>Dipartimento di Fisica e INFN, Università di Padova, via Marzolo 8, Padova, Italy

<sup>3</sup>Institute for Particle Physics, ETH Hönggerberg, Zürich, Switzerland

<sup>4</sup>Institute of Experimental Physics, Warsaw University, Warszawa, Poland

<sup>5</sup>Dipartimento di Fisica e INFN, Università di Milano, via Celoria 16, Milano, Italy

<sup>6</sup>Dipartimento di Fisica e INFN, Università di Pavia, via Bassi 6, Pavia, Italy

<sup>7</sup>Politecnico di Milano (CESNF), Università di Milano, via Ponzio 34/3, Milano, Italy

<sup>8</sup>Dipartimento di Fisica e INFN, Università dell'Aquila, via Vetoio, L'Aquila, Italy

<sup>9</sup>CERN, CH 1211 Geneva 23, Switzerland

<sup>10</sup>IHEP – Academia Sinica, 19 Yuqnan Road, Beijing, People's Republic of China

<sup>11</sup>Department of Physics, UCLA, Los Angeles, CA 90024, USA

<sup>12</sup>H.Niewodniczański Institute of Nuclear Physics, Kraków, Poland

<sup>13</sup>Institute of Physics, University of Silesia, Katowice, Poland

<sup>14</sup>Institute of Theoretical Physics, Wrocław University, Wrocław, Poland

<sup>15</sup>A.Soltan Institute for Nuclear Studies, Warszawa, Poland

<sup>16</sup>Faculty of Physics and Nuclear Techniques, University of Mining and Metallurgy, Kraków, Poland

<sup>17</sup>University of Torino, Torino, Italy

<sup>18</sup>INFN Pisa, via Livornese 1291, San Piero a Grado (PI), Italy

<sup>19</sup>Institute of Physics, Jagellonian University, Kraków, Poland

<sup>†</sup>Also at Dipartimento di Fisica e INFN, Università di Milano, via Celoria 16, Milano, Italy

<sup>‡</sup>Also at Laboratori Nazionali di Frascati, INFN, Frascati, Italy and Istituto di Cosmogeofisica, CNR, Torino, Italy

Italy

<sup>§</sup>Also at Dipartimento di Fisica e INFN, Università di Padova, via Marzolo 8, Padova, Italy

<sup>¶</sup>Spokesman

## Abstract

The final phase of the ICARUS physics program requires a sensitive mass of liquid Argon of 5000 tons or more. This is still true today, even after the operation of large or the planning of even larger underground detectors. The superior bubble-chamber-like features of the ICARUS detector will always provide additional and fundamental contributions to the field.

The most conservative way to reach a liquid Argon sensitive mass of 5000 tons is to start with a first prototype of a modest mass: the T600 detector. This step-wise strategy allowed us to develop progressively the necessary know-how to build a large liquid Argon detector.

The T600 detector stands today as the first living proof that such large detector can be built and that liquid Argon imaging technology can be implemented on such large scales.

After the successful completion of a series of technical tests to be performed at the assembly hall in Pavia, the T600 detector will be ready to be transported into the LNGS tunnel. The operation of the T600 at the LNGS will allow us (1) to develop the local infrastructure needed to operate our large detector (2) to start the handling of the underground liquid argon technology (3) to study the local background (4) to start the data taking with an initial liquid argon mass that will reach in a 5-6 year program the multi-kton goal. The T600 is to be considered as the first milestone on the road towards a total sensitive mass of 5000 tons: it is the first piece of the detector to be complemented by further modules of appropriate size and dimensions, in order to reach in a most efficient and rapid way the final design mass.

In this document, we describe the physics program that will be accomplished within the first phase of the program.

## 1 Introduction

The ICARUS physics program has been described in Volume I of the 1994 proposal [1]. The entire physics community has largely endorsed its physics goals, since Japan, America and also Europe have set up many programs with similar purposes, and much progress has been achieved in the field.

As already described in the original proposal, the final phase of the ICARUS project requires a sensitive mass of liquid Argon of 5000 tons or more. This is still true today, even after the advent of the SuperKamiokande with its fiducial mass of 22.5 ktons [2]. The superior bubble-chamber-like features of the ICARUS detector will provide additional and fundamental contributions to the field.

Back in 1995, it was decided that the most conservative way to reach the liquid Argon sensitive mass of 5000 tons was to go through a first step: the T600 detector [3]. This step-wise strategy allowed us to develop progressively the necessary know-how to build a large liquid Argon detector.

As a yet additional step, a large  $10m^3$  prototype was built in 1997, in order to assess the major issues concerning cryogenics, internal detector mechanics and liquid Argon purification. The  $10m^3$  prototype has undergone several cooling and filling tests in Pavia; this phase successfully ended in July 1999. The  $10m^3$  was then dismantled and transported to an external hall of LNGS. Complementing the dewar with appropriate H.V., wire readout, a scintillation light detection system and an external trigger, turned the prototype into a fully functional liquid Argon imaging chamber. A test, that lasted about 100 consecutive days, has allowed to prove the technique in a configuration similar to the one adopted for the T600 detector and, thanks to a perfectly mastered LAr purification technique, has resulted in the collection of ionizing events of excellent quality.

The T600 detector stands today as the first living proof that a large detector can be built and that liquid Argon imaging technology can be implemented on such large scales. We are now

ready to propose the construction of a second T600 “clone”, within a 24 months program, to complete within 2003 the first 35 meters of the experimental hall, with 1.2 kton of active liquid Argon mass.

After the successful completion of a series of technical tests to be performed at the assembly hall in Pavia, the T600 detector will be ready to be transported into the LNGS tunnel.

The operation of the T600 at the LNGS will allow us (1) to develop the local infrastructure needed to operate our large detector (2) to start the handling of the underground liquid argon technology (3) to study the local background (4) to start the data taking with an initial liquid argon mass that will reach in a 5-6 year program the multi-kton goal. The T600 is to be considered as the first milestone on the road towards a total sensitive mass of 5000 tons: it is the first piece of the detector to be complemented by further modules of appropriate size and dimensions, in order to reach in a most efficient and rapid way the final design mass.

In this document, we describe the physics program that will be accomplishable with the first modules of liquid Argon. Given this initial phase in which a limited amount of liquid Argon is available, we consider the physics program achievable with exposures of 1 or 2 kton  $\times$  year.

In section 2, we discuss the benchmark measurement provided by the detection of downward-going muons. In section 3, we address the detection of atmospheric neutrinos, including fully-contained and partially-contained events, and upward going muons. In section 4 the detection of solar neutrinos is discussed. The sensitivity to nucleon decays is explored in section 5. Finally, the detection of supernova neutrinos is treated in section 6.

## 2 Detection Of Downward-Going Muons

The rock overburden at Gran Sasso underground laboratory filters secondary cosmic ray particles produced in atmospheric showers, and only high energy muons (coming from the decay of secondary  $\pi$  and K mesons) survive, with a rate of about 1 particle /m<sup>2</sup> hour. The energy threshold for an atmospheric muon to reach the underground hall has an exponential dependence on the rock depth  $h(\theta, \phi)$  [4], which is a function of the direction, depending on the mountain topography. In correspondence of the minimum thickness ( $\sim 3100$  hg/cm<sup>2</sup>, in the direction of Campo Imperatore)  $E_{thr} \sim 1.3$  TeV. The average residual energy of muons at the depth of Gran Sasso underground hall is about 300 GeV. In their propagation through the rock muons undergo different interaction processes affecting also their direction. The average scattering angle has been calculated to be around 1 degree, mostly dominated by multiple scattering in the last part of their path.

The measurement of atmospheric muons surviving underground is not a primary goal of ICARUS. However, it can be considered a benchmark test of the detector performance, but also an interesting by-product of the physics research program. As a matter of fact, muons are practically the only available high energy particles with a quite constant rate which can be used to perform an effective monitoring of the detector performance as far as track reconstruction is concerned. An example of a possible measurement is that of the muon flux as a function of the rock depth, or “depth-intensity” function  $I(h)$ . The comparison with the world average of  $I(h)$  [5], and in particular with the results from the previous experiments at Gran Sasso [6, 7], provides a check of the efficiency and stability of the detector operation. Such a measurement requires a precise knowledge of the detector acceptance and in addition, is a good check of the detector simulation codes.

From the physics point of view, the measurement of the underground muon flux allows, by means of a detailed simulation of atmospheric showers, to extract the parameters of the all-nucleon flux of primary cosmic rays, in the region around a few TeV/nucleon, where also

direct measurements suffer of large errors. A better knowledge of the primary flux in this energy region is still important to reduce uncertainties in the calculations of the flux of atmospheric neutrinos. The main interest is in a new analysis, more than in the statistics, which has been largely collected by MACRO and LVD, since the interpretation is limited by both, theoretical systematics (hadronic interaction models) and the knowledge of rock depth. At present, Gran Sasso rock is known with an accuracy which is not better than a few percent. Furthermore, further measurements at large zenith angle, *i.e.* at very large values of  $h(\theta, \phi)$ , where the rate is quite low, are important to extract informations about prompt muon production, connected to the charm production in atmospheric showers [4]. Also, the measurement close to the horizontal direction is known to be dominated by atmospheric neutrino interaction in the rock, and it is useful to establish the  $\nu$  flux normalization in a direction where the oscillation phenomena, according to the present estimate of parameters, are marginal. In this large zenith angular region, the contribution of new data is in any case important and ICARUS has at least a clear advantage, for instance, with respect to MACRO, which did not present a specific analysis in this field.

In order to evaluate the rate of downward-going muons detectable in the T600 module, we have performed a full simulation in the FLUKA environment [8, 9], assuming that the module is located in the Hall B of the Gran Sasso underground laboratory. In order to generate the local muon flux, a  $\cos(\text{zenith}) - \phi$  matrix, unfolded from the MACRO experimental data, has been used. For this first iteration of this kind of calculation, the contribution of multiple muon events (about 6% of the total muon event rate) has been neglected. To identify a muon, we require a track of at least 20 cm, passing through at least one half-module. The experience gained with the operation of the 10 m<sup>3</sup> module [11] allows us to have confidence that, with this minimum track length, a 3-Dimensional reconstruction is fully assured (at least 40–50 hits/view). In this way we expect to detect 120 tracks/hour. The expected angular distribution, the shape of which is dominated by the rock overburden, is reported in Fig.1<sup>1</sup>.

Within one year of live time, the data collected by the T600 module would reach half the statistics collected by LVD in [6].

From the above angular distribution the bin-by-bin muon intensity  $I(h)$  referred to the vertical direction is extracted as follows:

$$I(h) = \left( \frac{1}{\Delta T} \right) \frac{\sum_i N_i m_i}{\sum_j \Delta \Omega_j A_j \epsilon_j / f \theta_j} \quad (1)$$

where  $\Delta T$  is the live time;  $N_i$  is the number of observed events of muon multiplicity  $m_i$  in the bin of slant depth  $h$ ;  $A_j$  is the effective detector projected area for that bin;  $\epsilon_j$  is the combined trigger and reconstruction efficiency and  $\theta_j$  is the muon zenith angle. The function  $1/f\theta_j$  represents the zenith distribution of muons in the atmosphere, which, for these energies and up to 60°, is well approximated by  $\sec\theta_j$ . For larger angles corrections must be introduced to take into account the earth's curvature. The projected area  $A_j(\theta, \phi)$  and the detector tracking efficiency  $\epsilon_j(\theta, \phi)$  must be calculated from a detailed Monte Carlo study. In order to compare experimental results from different sites, it is customary to convert the actual rock thickness to “standard rock” ( $Z=11$ ,  $A=22$ ) slant depth, using the known chemical composition of the Gran Sasso rock and a conversion formula, like the one described in [10].

The topic of the study of atmospheric muons includes other items which can be of interest for ICARUS. In addition to the test runs foreseen in Pavia, the run of the T600 module in

---

<sup>1</sup>There the  $\phi$  angle is measured counter-clockwise from the axis parallel to the longitudinal section of Hall B, which makes an angle of 128.4° with respect to the geographical North. The azimuth angle is normally defined as the angle measured clockwise from the North direction.

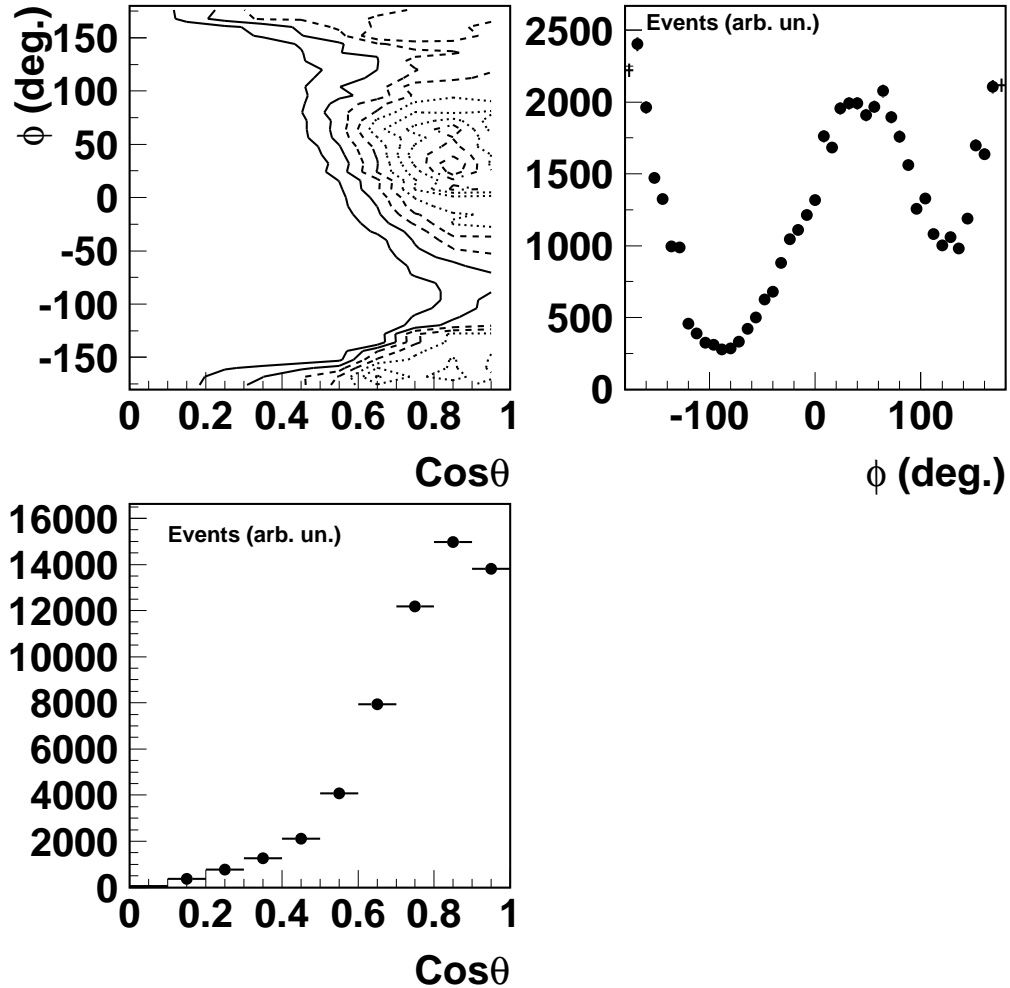


Figure 1: Expected angular distribution of downward-going muons detected in the T600 module.

Gran Sasso is necessary to study the analysis techniques. Briefly we can mention the following arguments:

1. Study of multiple muon events, which brings information about the mass composition of primary cosmic rays. A fundamental advantage with respect to the work performed by previous experiments, like MACRO [12], would be the possibility of reducing the error in the multiplicity determination of the largest events, thanks to the fine grain spatial resolution. In fact, the highest multiplicity events are found to be often composed of close tracks, concentrated in a relatively small area.
2. Study of the local energy spectrum of muons, exploiting the technique of energy evaluation of muon tracks by means of the multiple scattering evolution.
3. Detailed study of radiative and photonuclear interactions of high energy muons in the liquid Argon.

## 3 Atmospheric Neutrinos

### 3.1 Contained and partially contained events

The comprehensive investigation of atmospheric neutrino events, beyond what was already achieved in SuperKamiokande, requires a fiducial mass of several ktons, in order to reach the level of at least one thousand events per year. The physics goals of new atmospheric neutrino measurements are to firmly establish the phenomenon of neutrino oscillations with a different experimental technique, possibly free of systematic biases, measure the oscillation parameters and clarify the nature of the oscillation mechanism.

The statistics accumulated in a 2 kton  $\times$  year exposure will be modest (see Table 1). They will be comparable to those obtained in the first generation of water Cerenkov detectors, namely Kamiokande and IMB.

The capability to observe all processes, electron, muon and tau neutrino charged current events (CC) and all neutral currents (NC) without detector biases and down to kinematical threshold, will however provide an unique new view on the atmospheric events.

The ICARUS T600 will offer an observation of atmospheric neutrinos of a very high quality, thanks to its unique performance in terms of resolution and precision.

The perspective of ICARUS is to provide redundant, high precision measurement and minimize as much as possible the systematics uncertainties of experimental origin which affect the results of existing experiments. Improvements over existing methods are expected in

1. neutrino event selection
2. identification of  $\nu_\mu$ ,  $\nu_e$  and  $\nu_\tau$  flavors
3. identification of neutral currents

The operation of the T600 will be the only way to demonstrate *in situ* the expected performance of the liquid Argon technique.

Unlike measurements obtained up to now in Water Cerenkov detectors, which are in practice limited to the analysis of “single-ring” events, complicated final states with multi-pion products, occurring mostly at energies higher than a few GeV, will be completely analyzed and reconstructed in the T600. This will be a significant improvement with respect to previous observations. As an example, we anticipate a much better angular resolution of the reconstructed direction of the incoming neutrino. The reconstruction of the zenith angle of the incoming  $\nu$  is of great importance in the search of oscillations in atmospheric neutrinos. In SuperKamiokande measurements, the direction of the incoming neutrino is taken to be the one of the leading lepton, since due to pattern recognition, only single “ring” events are analyzed. ICARUS allows for a better reconstruction of the incoming neutrino variables (i.e. incidence angle, energy) by using the information coming from all particles produced in the final state.

Figure 2(left) shows the distribution of the difference between the real and reconstructed neutrino angle for the whole sample of events with  $E_\nu > 1$  GeV. The improvement on the angular resolution is visible. The RMS of the distribution improves from  $\sim 16$  to  $\sim 8$  degrees after the inclusion of the hadronic jet in the reconstruction.

Figure 2(right) shows the zenith angle resolution as a function of the incoming neutrino energy, comparing the two methods of reconstruction. For energies tending to zero, the resolution is dominated by the smearing introduced by the Fermi motion of the initial state nucleon and by re-interaction of the hadrons inside the nucleus, and therefore the improvement obtained with the hadronic jet is minimal. For energies above  $\approx 500$  MeV, the improvement in resolution is significant. It should be noted that at higher energies, the inclusion of the hadronic jet improves

	2 kton×year				
	No osci	$\Delta m_{23}^2$ (eV <sup>2</sup> )			
		$5 \times 10^{-4}$	$1 \times 10^{-3}$	$3.5 \times 10^{-3}$	$5 \times 10^{-3}$
<b>Muon-like</b>	$270 \pm 16$	$206 \pm 14$	$198 \pm 14$	$188 \pm 14$	$182 \pm 13$
Contained	$134 \pm 12$	$100 \pm 10$	$96 \pm 10$	$88 \pm 9$	$86 \pm 9$
Partially-Contained	$136 \pm 12$	$106 \pm 10$	$102 \pm 10$	$100 \pm 10$	$96 \pm 10$
No proton	$104 \pm 10$	$76 \pm 9$	$74 \pm 9$	$68 \pm 8$	$66 \pm 8$
One proton	$82 \pm 9$	$64 \pm 8$	$60 \pm 8$	$58 \pm 8$	$56 \pm 7$
Multi-prong	$84 \pm 9$	$66 \pm 8$	$64 \pm 8$	$62 \pm 8$	$60 \pm 8$
$P_{lepton} < 400$ MeV	$114 \pm 11$	$82 \pm 9$	$80 \pm 9$	$74 \pm 9$	$70 \pm 8$
$P_{lepton} \geq 400$ MeV	$156 \pm 12$	$124 \pm 11$	$118 \pm 11$	$114 \pm 11$	$112 \pm 11$
<b>Electron-like</b>	$152 \pm 12$	$152 \pm 12$	$152 \pm 12$	$152 \pm 12$	$152 \pm 12$
Contained	$100 \pm 10$	$100 \pm 10$	$100 \pm 10$	$100 \pm 10$	$100 \pm 10$
Partially-Contained	$52 \pm 7$	$52 \pm 7$	$52 \pm 7$	$52 \pm 7$	$52 \pm 7$
No proton	$64 \pm 8$	$64 \pm 8$	$64 \pm 8$	$64 \pm 8$	$64 \pm 8$
One proton	$48 \pm 7$	$48 \pm 7$	$48 \pm 7$	$48 \pm 7$	$48 \pm 7$
Multi-prong	$40 \pm 6$	$40 \pm 6$	$40 \pm 6$	$40 \pm 6$	$40 \pm 6$
$P_{lepton} < 400$ MeV	$74 \pm 9$	$74 \pm 9$	$74 \pm 9$	$74 \pm 9$	$74 \pm 9$
$P_{lepton} \geq 400$ MeV	$78 \pm 9$	$78 \pm 9$	$78 \pm 9$	$78 \pm 9$	$78 \pm 9$
<b>NC-like</b>	$192 \pm 14$	$192 \pm 14$	$192 \pm 14$	$192 \pm 14$	$192 \pm 14$
<b>TOTAL</b>	$614 \pm 25$				

Table 1: Expected atmospheric neutrino rates in case no oscillations occur and assuming  $\nu_\mu \rightarrow \nu_\tau$  oscillations take place with maximal mixing. Four different  $\Delta m^2$  values have been considered. Only statistical errors are quoted.

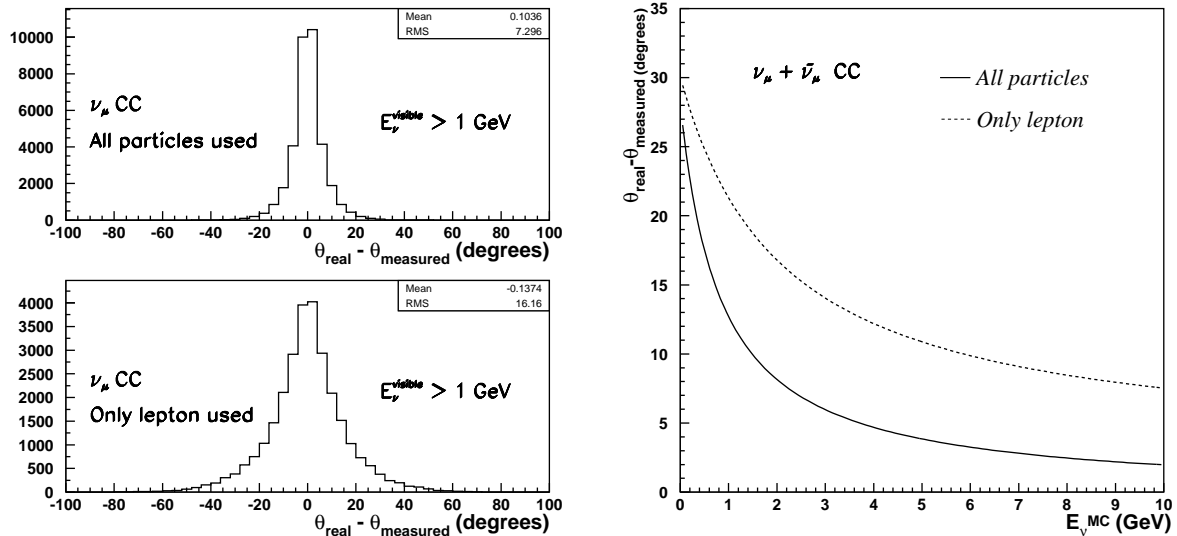


Figure 2: (left) Zenith angle resolution. The top plot shows the resolution obtained by reconstructing the incoming neutrino direction using all particles momenta, the bottom plot shows the resolution obtained using only the leading lepton momentum. (right) Zenith angle resolution as a function of the neutrino energy.

by a factor three the reconstruction of incoming neutrino direction. This will allow to have a more precise reconstruction of the neutrino L/E (see ICANOE proposal [13]).

We recall the expected atmospheric neutrino rates obtained per year for an exposure of 2 ktons in Table 1, with and without  $\nu_\mu \rightarrow \nu_\tau$  oscillation hypothesis ( $\sin^2 2\theta = 1$ ).

Muon-like events contain an identified muon and correspond to  $\nu_\mu/\bar{\nu}_\mu$  CC events. Electron-like are events with an identified electron and are  $\nu_e/\bar{\nu}_e$  CC events. Given the clean event reconstruction, the ratio  $R$  of “muon-like” to “electron-like” events can be determined free of large experimental systematic errors. In fact, the expected purity of the samples is above 99%. In particular, the contamination from  $\pi^0$  in the “electron-like” sample is expected to be completely negligible.

We further split the muon and electron-like events into fully-contained and partially-contained samples. “Fully contained events” are those for which the visible products of the neutrino interaction are completely contained within the detector volume. “Partially contained events” are events for which the leading lepton exits the detector volume. Figure 3 shows the containment of charged current events for different incoming neutrino energies and leading lepton momentum thresholds. The top plot refers to  $\nu_\mu + \bar{\nu}_\mu$  CC events and the bottom plot to  $\nu_e + \bar{\nu}_e$  CC. In the computation, events were generated uniformly over the full T600 active argon volume and were oriented correctly in the detector volume. Particles were tracked through the argon until they reached the wall of the argon volume.

Muon-like events are less contained than electron-like ones. The overall fraction of contained events is 50% for  $\nu_\mu + \bar{\nu}_\mu$  CC events. This fraction decreases rapidly with muon momentum. For muon momenta above 2 GeV, in practice, all muons will escape the mother volume. Since at low energies, muons carry on the average more than half of the incoming neutrino energy, this strong dependence of the containment is also visible as a function of the incoming neutrino



energy (see Figure 3, top plot). The fraction of contained  $\nu_e + \bar{\nu}_e$  CC is close to 70% of the total expected rate. The decrease of containment with energy is not so dramatic for electron-like events. For neutrino energies in excess of 5 GeV, we expect half of the  $\nu_e + \bar{\nu}_e$  CC sample to be fully contained (see Figure 3, bottom plot).

For the muon-like contained events, the muon energy is precisely determined by integration of the  $dE/dx$  measurements along the track. For partially contained events, in which the muon escapes the detector active volume, the muon momentum is estimated via the multiple scattering method (see ICAROE proposal [13]). Fully contained electromagnetic showers are extremely well measured thanks to the superb calorimetric performance of liquid Argon. The energy of partially contained showers can be recovered by a careful “shower-shape” analysis.

We also illustrate the expected event rates classified according to their final state multiplicity (see Table 1). Approximately 40% of CC events contain no proton in the final state<sup>2</sup>, corresponding to the “one-ring” sample. The rest of the events will contain a proton or multi-prongs final states, which will provide, thanks to the precise reconstruction of all particles, a precise determination of the incoming neutrino energy and direction.

Finally, we also point out that in ICARUS atmospheric neutrino events can be analyzed down to production threshold, given the excellent imaging. We illustrate this by classifying the events according to the energy of the leading lepton (electron or muon). We split the samples into  $P_{lepton} < 400$  MeV and  $P_{lepton} > 400$  MeV, which correspond to the threshold used in Super-Kamiokande [2]. Almost 50% of the expected rate lies below the threshold and hence ICARUS can really contribute to the understanding of the low energy part of the atmospheric neutrino spectrum.

An improved observation of about 100 neutral current (NC) events per kton  $\times$  year is also expected, given the clean classification of events based on the absence of an electron or muon in the final state. In this case, the excellent  $e/\pi^0$  separation plays a fundamental role to select an unbiased, free of background neutral current sample.

	2 kton $\times$ year				
	No osci	$\Delta m_{23}^2$ (eV <sup>2</sup> )			
		$5 \times 10^{-4}$	$1 \times 10^{-3}$	$3.5 \times 10^{-3}$	$5 \times 10^{-3}$
<b>Muon-like</b>	$270 \pm 16$	$206 \pm 14$	$198 \pm 14$	$188 \pm 14$	$182 \pm 13$
Downward	$102 \pm 10$	$102 \pm 10$	$102 \pm 10$	$98 \pm 10$	$95 \pm 10$
Upward	$94 \pm 10$	$46 \pm 7$	$46 \pm 7$	$47 \pm 7$	$49 \pm 7$
<b>Electron-like</b>	$152 \pm 12$	$152 \pm 12$	$152 \pm 12$	$152 \pm 12$	$152 \pm 12$
Downward	$56 \pm 7$	$56 \pm 7$	$56 \pm 7$	$56 \pm 7$	$56 \pm 7$
Upward	$48 \pm 7$	$48 \pm 7$	$48 \pm 7$	$48 \pm 7$	$48 \pm 7$

Table 2: Predicted downward ( $\cos \theta_{zenith} > 0.2$ ) and upward ( $\cos \theta_{zenith} < -0.2$ ) atmospheric neutrino rates in case no oscillations occur and assuming  $\nu_\mu \rightarrow \nu_\tau$  oscillations take place with maximal mixing. Four different  $\Delta m^2$  values have been considered. Only statistical errors are quoted. As a reference, we also show the total expected rates for both muon and electron-like events.

<sup>2</sup>A proton is identified if its kinetic energy is above 50 MeV.

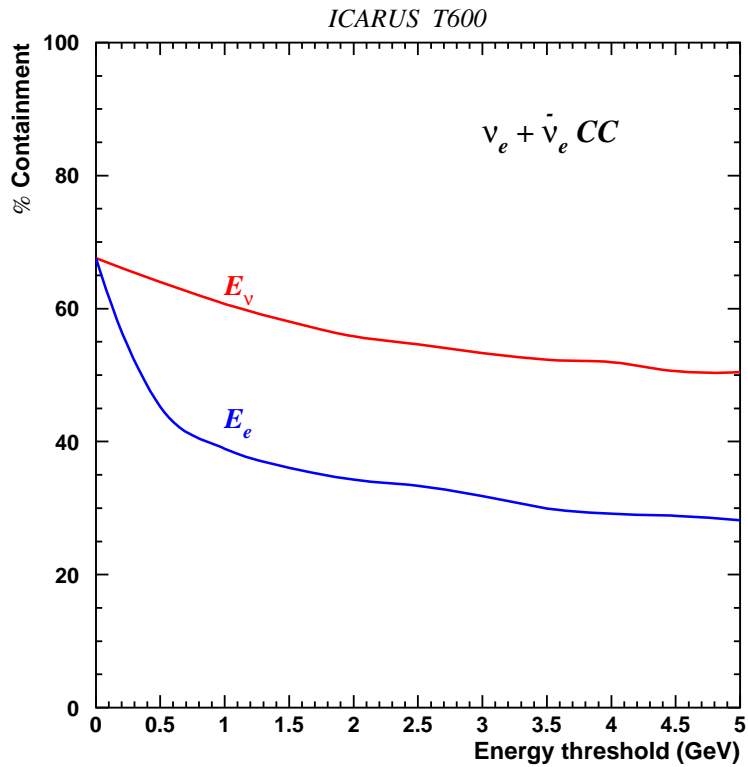
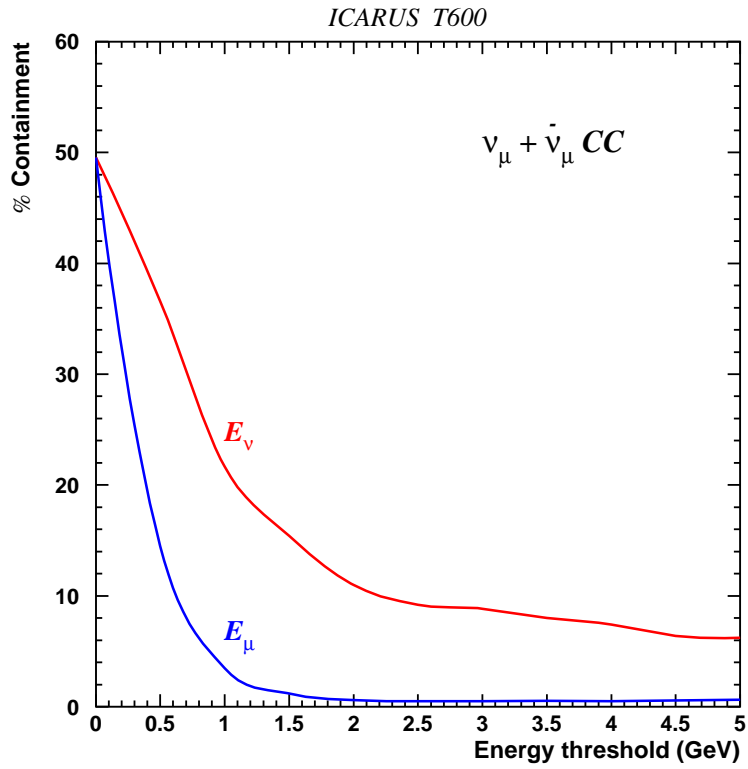


Figure 3: Integral distributions showing the containment for CC events as a function of the neutrino energy and the leading lepton momentum. Top plot:  $\nu_\mu + \bar{\nu}_\mu$  CC. Bottom plot:  $\nu_e + \bar{\nu}_e$  CC.

The presence of neutrino oscillations leads to differences in the predicted rates of upward and downward going neutrino events (see Table 2). For a 2 kton  $\times$  year exposure, we will measure a quite evident deficit of upward-going muon-like events, for the range of oscillation parameters presently allowed by Super-Kamiokande measurements.

The question whether the atmospheric neutrino anomaly is due to  $\nu_\mu \rightarrow \nu_\tau$  or  $\nu_\mu \rightarrow \nu_s$  oscillations is not totally settled [14]. The clean NC sample will allow us to perform an “indirect”  $\nu_\tau$  appearance search. To discriminate between  $\nu_\mu \rightarrow \nu_\tau$  and  $\nu_\mu \rightarrow \nu_s$  oscillations, we measure the ratio  $R_{NC/e} = \frac{NC^{obs}/\nu_e CC^{obs}}{NC^{exp}/\nu_e CC^{exp}}$ . An oscillation to an active neutrino leads to  $R_{NC/e} = 1$ , while  $R_{NC/e} \sim 0.7$  is expected for an oscillation to a sterile neutrino.

The value and error of  $R_{NC/e}$ , in case of oscillation to active neutrino, are shown in Table 3, either using all events or only fully contained ones. The systematic error is expected to be low, since our measurement of the double ratio does not depend on poorly known cross sections (e.g., single  $\pi^0$  production). The expected error on  $R_{NC/e}$  is 22% (15%) for an exposure of 1 (2) kton  $\times$  year. The quoted uncertainty is similar to the one obtained by Super-Kamiokande (which is strongly dominated by systematics).

Exposure (kton $\times$ year)	$R_{NC/e}$	
	all events	contained
1	$1.0 \pm 0.22$	$1.0 \pm 0.23$
2	$1.0 \pm 0.15$	$1.0 \pm 0.16$
5	$1.0 \pm 0.10$	$1.0 \pm 0.10$

Table 3:  $R_{NC/e}$  as a function of the exposure assuming oscillation to an active neutrino. Quoted errors are of statistical nature.

### 3.2 Upward-Going Muons

Muon neutrinos undergoing CC interactions in the rock surrounding the detector can produce muon tracks detectable by the apparatus. These events are produced by neutrinos belonging to an energy region which is higher with respect to that of contained or partially contained events: typically they cover the range from Multi-GeV up to few TeVs, with a maximum in the region around 100 GeV. Therefore they are an interesting complement to the analysis of atmospheric neutrinos, since the disappearance due to the oscillation process (or other disappearance mechanisms) will be quantitatively different with respect to contained, or partially contained events. Furthermore, these events are also affected by different systematics, not only because they belong to a different region of the spectrum, but also because of different cross sections and target material (the rock).

Upward-going muons allow to explore path lengths through the Earth ranging from few hundred km up to  $\sim 13000$  km. Neutrino oscillation will modify the total number of events and their zenith angle distribution, mostly around the vertical direction, as already discussed in the work of Super-Kamiokande [16] and MACRO [15]. Furthermore, the analysis of the angular distribution of upward-going muons is one of the tools to discriminate between  $\nu_\mu\text{-}\nu_s$  and  $\nu_\mu\text{-}\nu_\tau$  oscillations [17].

It is clear that the T600 module is not large enough to provide statistically competitive results with respect to MACRO or Super-Kamiokande. Instead, its operation at Gran Sasso allows to test a specific capability of ICARUS to recognize track direction, thanks to the fine spatial resolution, which allows to identify and reconstruct  $\delta$ -rays produced along the track.

If an energy cut is applied in order to select sufficiently energetic  $\delta$  electrons, then these are expected to be emitted in the direction of the parent. In fact, the cosine of the angle  $\Theta$  between the  $\delta$  and the primary muon, for energies much larger than the atomic levels, is given by the following expression:

$$\cos \Theta = \frac{T_e}{P_e} \frac{(E_\mu - m_e)}{P_\mu} \quad (2)$$

where  $T_e$  and  $P_e$  are the kinetic energy and the momentum of the emitted electron,  $E_\mu$  and  $P_\mu$  are the total energy and the momentum of the parent muon and  $m_e$  is the electron mass.

Therefore, practically independently of  $E_\mu$ ,  $\delta$  electrons of a few MeV are emitted at small angle. Requiring a threshold of 10 MeV, about one  $\delta$  ray of this kind is produced for each meter of track. An electron of 10 MeV has a range slightly exceeding 5 cm, and, with the wire pitch of 3 mm, its track can be sampled 15 times. The multiple scattering in argon will be relevant only at the end of  $\delta$  electron range, while in the first part of the track, the multiple scattering  $\theta^{rms} \sim 5^\circ$  in one cm. In order to have a good rejection power, it is therefore necessary to ask for a minimum track length of 2÷3 m, with at least 2  $\delta$ 's above threshold. Monte Carlo simulations show that this method allows to achieve the required rejection power. In the case of low energy muons, a redundant method to identify the direction can come from the analysis of the evolution of the multiple scattering angle along the track.

### 3.2.1 Experimental test with the 50 liter prototype

In order to perform a test of the actual reconstruction ability of the  $\delta$ -rays direction on real muon tracks, we took advantage of the data taken with the ICARUS 50 liter LAr TPC exposed at the CERN neutrino beam during the 1997 physics run. The detector and the experimental set-up has been extensively described elsewhere [18]. The results discussed here come from a recent re-analysis of these data [19], which took advantage of the current developments on the reconstruction program.

The collected muon event sample (about one thousand) was used to study the possibility to exploit the visible  $\delta$ -rays to determine the direction of minimum ionizing particle tracks crossing the detector. It allowed us to verify on real data the minimum energy allowing full reconstruction of the  $\delta$ -ray direction and, as a consequence, the effective rate that one can finally expect.

The analysis proceeded through the following steps. The whole sample of through-going minimum ionizing particle tracks was visually scanned. Only the events containing a muon fully reconstructed in NOMAD and matching a track in the LAr-TPC were retained. This requirement safely predefined the direction of the selected tracks in the LAr-TPC.

The selected muon sample consists of 320 events, corresponding to 120 m of minimum ionizing particle track. The search and reconstruction of  $\delta$ -rays were then performed following a series of simple criteria. A visible  $\delta$ -ray was defined as a track starting as double ionization on top of the main muon track and stopping aside of the main track in at least one view.

The  $\delta$ -ray kinetic energy was simply calculated from the reconstructed 3-D range of its track, knowing that the average  $dE/dx$  is about 2.1 MeV/cm practically constant over all the range. Only  $\delta$ -rays with deposited energy above 2 MeV and below 30 MeV (critical energy in LAr) were retained.

The above criteria selected 235  $\delta$ -rays over the total 120 meters of tracks, namely about 2  $\delta$ -rays per meter, with kinetic energy larger than 2 MeV. Remarkably, none was identified with the wrong direction.

In order to understand our results, we compared the experimental  $\delta$ -rays energy spectrum with the predicted rate, valid for kinetic energy much higher than the mean excitation energy

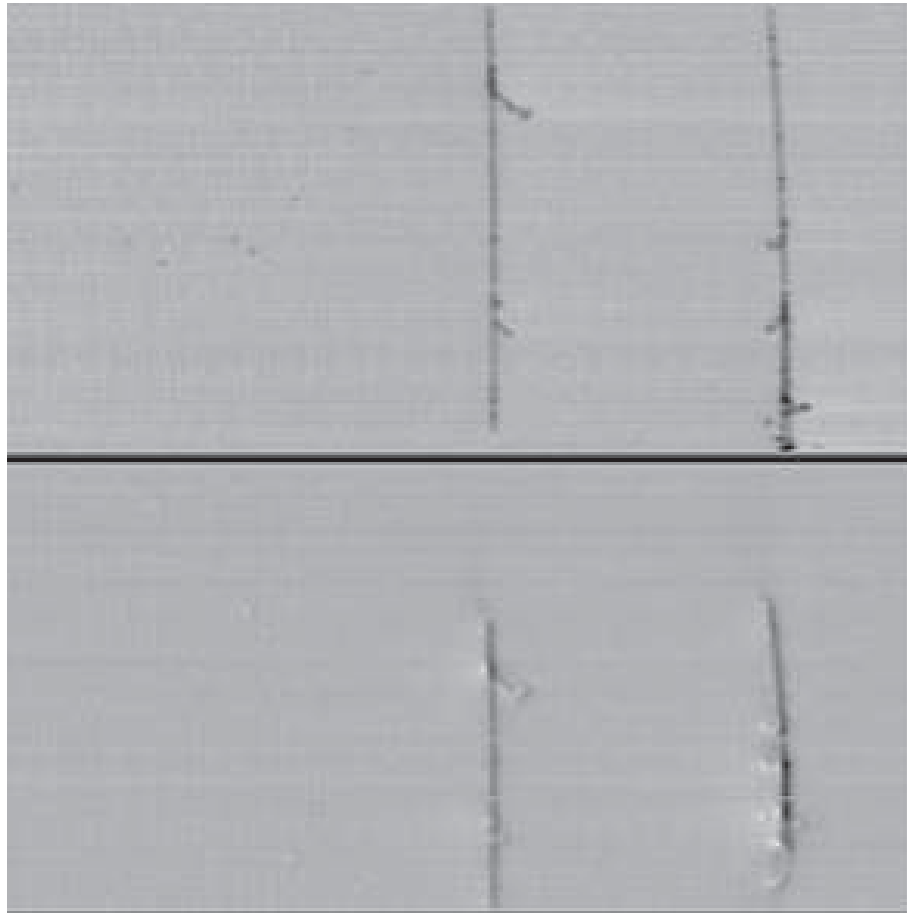


Figure 4: An example of muon track recorded in the ICARUS 50 liter liquid Argon TPC prototype exposed at the CERN neutrino beam. The horizontal axis is the drift time; the vertical one is the wire numbering (top is the collection view, bottom is the induction plan). The visible area in each view corresponds to  $472 \times 325 \text{ mm}^2$ . The muon enters from the top of the picture on both views. Some  $\delta$ -rays are clearly visible. The track at the extreme right of the picture is not matched by NOMAD and exhibits a showering electron.

( $T \gg 188$  eV for Argon) [20]:

$$\frac{d^2 N}{dT dx} \approx \frac{1}{2} K \rho \frac{Z}{A} \frac{1}{\beta^2} \frac{1}{T^2} F_1 F_2 \quad (3)$$

$$= \frac{9.67 F_1 F_2}{(T/MeV)^2} m^{-1} MeV^{-1} \quad (4)$$

To account for the selection requirements two factors,  $F_1$ ,  $F_2$ , were included in Equation 4. The containment factor,  $F_1$ , was used to account for the fact that not all the muon track length was available as origin of a  $\delta$ -ray because a fraction of it was needed to contain the  $\delta$ -ray.  $F_1$  decreases with increasing  $\delta$ -ray energy.

The fraction of events, the end-point of which was separated from the muon track by more than 6 mm in at least one of the two 2-D views, was evaluated by means of the multiple scattering formula. The separation factor,  $F_2$ , was thus computed as a function of the kinetic energy of the  $\delta$ -rays.  $F_2$  increases with increasing  $\delta$ -ray energy.

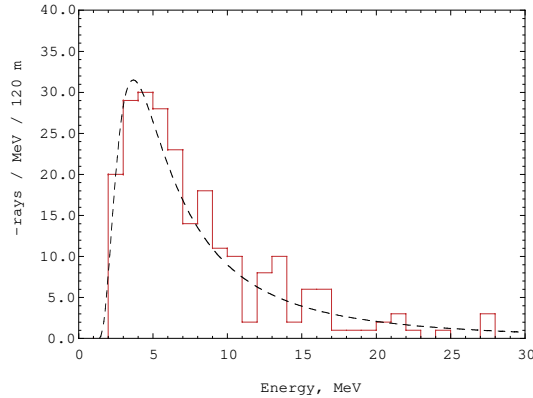


Figure 5: Energy distribution of the  $\delta$ -rays: experimental data (solid histogram) are plotted together with the expected rate normalized to 120 m of m.i.p. track (dashed curve).

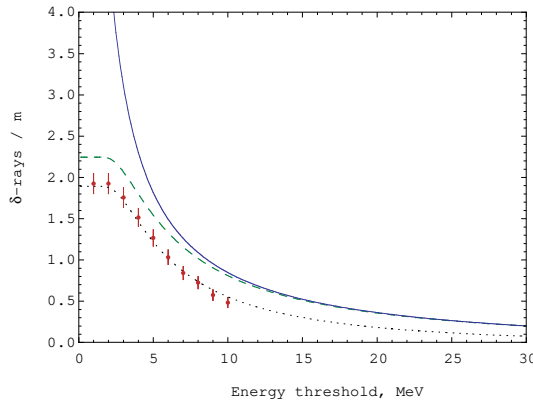


Figure 6: Experimental cumulative energy distribution of the  $\delta$ -rays (solid circles). The expectations are also plotted: the solid curve gives the rate with no selection cuts, the dotted line takes into account the factors  $F_1$  and  $F_2$  described in the text, the dashed one includes only  $F_2$ .

Figure 5 shows the energy spectrum of the experimental data of this test superimposed to that predicted with Equation 4 normalized to 120 meters of track. Note, that the maximum

rate occurs for a kinetic energy of 4 MeV and it decreases rapidly at low energy side because of the separation requirement.

Figure 6 shows the integrated  $\delta$ -ray spectrum as a function of the energy threshold normalized to one meter of track. Data are plotted together with the predictions. The solid curve gives the rate with no cuts. The dotted line instead takes into account the factors  $F_1$  and  $F_2$ : the agreement with the data is satisfactory.

The dashed line, which included only the factor  $F_2$ , has also been plotted because it gives the rate expected in a large LAr-TPC where the  $\delta$ -rays containment factor,  $F_1$ , is close to 100 %. About 2.25 reconstructed  $\delta$ -rays per meter of track are predicted with energy above 2 MeV.

We demonstrated experimentally that in the ICARUS LAr-TPC we could make use of the  $\delta$ -rays kinematics to determine the direction of a minimum ionizing particle track crossing the detector [19]. Slightly more than two  $\delta$ -rays per meter of track should be fully reconstructed. This implies that the ability to reconstruct track direction is very high: an efficiency of 99 % is at reach considering only 2 m of track.

### 3.2.2 Expected event rate at LNGS

We have considered a full simulation in the FLUKA environment [8, 9] of the 600 tons module of ICARUS. Upward-going muons have been generated with the local expected spectrum and angular distribution predicted by the Bartol model [21] and considering a statistics equivalent to 30 years of operation. A minimum track length of 2 meters has been requested. In the no-oscillation case, 37 events/year are expected in the T600 module. The additional requirement of producing at least 2  $\delta$ 's of energy greater or equal to 10 MeV reduces this number to 29 useful events.

$\Delta m^2$ ( $10^{-3} \text{ eV}^2$ )	Events/year
1	23
3	20
5	13

Table 4: Expected rate of reconstructed upward going muon events in the T600 module for a minimum track length of 2 m and asking for the identification of at least 2  $\delta$ s with  $E \geq 10$  MeV.

Table 4 summarizes these results for different values of the  $\Delta m^2$  oscillation parameter in the maximal mixing  $\nu_\mu$ - $\nu_\tau$  scenario.

The expected zenith angle distributions achievable in 2 years (live time) of operation for the different values of  $\Delta m^2$  are reported in Fig. 7

In addition, we can mention that the particle identification capability in the liquid Argon allows to have further rejection of the background due to upward-going charged hadrons locally produced in the interactions of downward-going muons [22].

## 4 Solar Neutrinos

The unique capabilities of a liquid Argon TPC are suitable to the real-time detection of the neutrinos produced in the Sun. Two independent neutrino reactions contribute to the total expected rate: elastic scattering by electrons and absorption on Argon nuclei. These

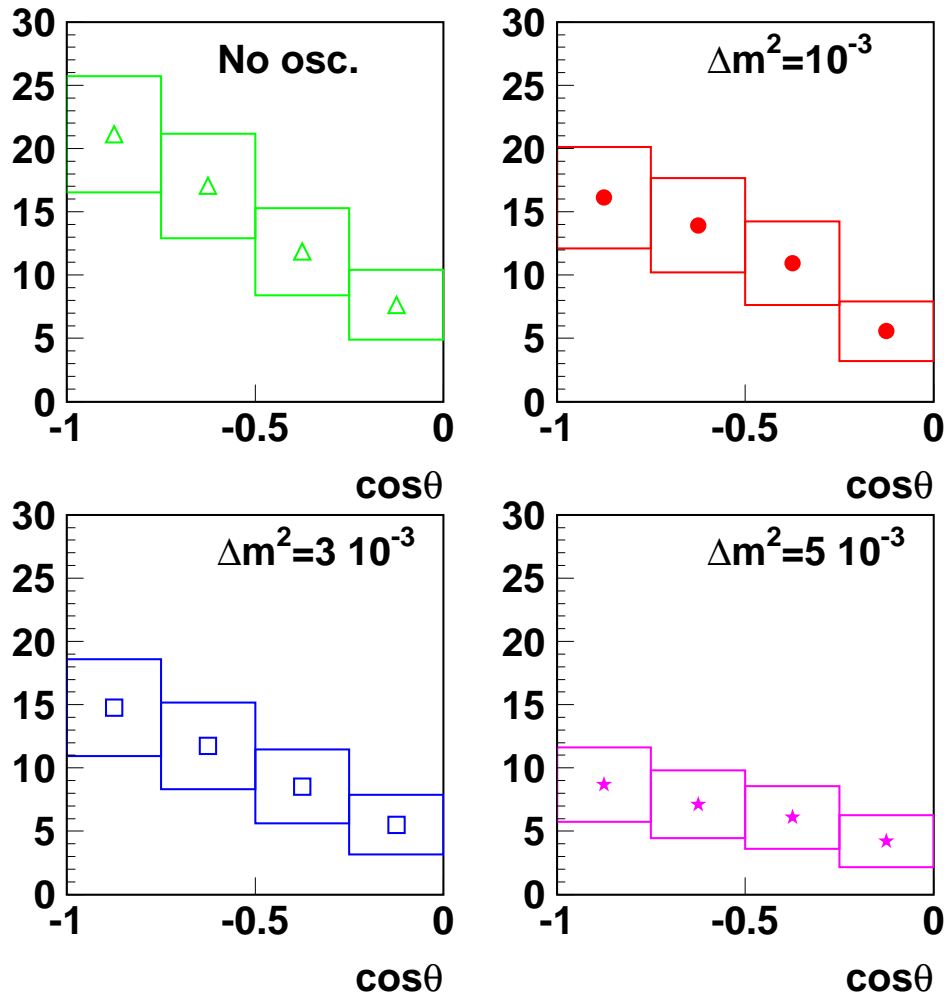


Figure 7: Expected zenith angle distributions achievable in 2 years (live time) of operation for the different values of  $\Delta m^2$  ( $\sin^2 2\theta = 1$ ) as a function of the cosine of the zenith angle. The box shows the statistical error.



interactions usually result in the production of a primary electron track, sometimes accompanied by secondary electron tracks of lower energy.

Small liquid Argon TPC prototypes have demonstrated that electrons with a kinetic energy as low as 150 keV can be detected [18]. This performance allows a detailed reconstruction of the solar neutrino interactions. The background induced by natural radioactivity and the need to establish the electron direction in elastic scattering events, require a threshold for the detection of primary electrons. As will be discussed below, this threshold is of the order of 5 MeV for elastic and absorption events, thus allowing investigation on the higher energy part of the solar neutrino spectrum ( $^8\text{B}$  and hep).

The performance of the ICARUS T600 detector in the analysis of solar neutrino events are widely discussed in a recent, dedicated ICARUS publication [23]. We only recall here the main results of this study, referring to the paper for the detailed analysis, in particular regarding the background estimate.

## 4.1 Event and background rates evaluation

ICARUS can make a fundamental contribution to our understanding of solar neutrino intensities and their energy spectrum, by observing the electron produced in the following independent processes:

- elastic scattering by electrons:  $\nu_{e,\mu,\tau} + e^- \rightarrow \nu_{e,\mu,\tau} + e^-$
- absorption reactions on Argon nuclei:  $\nu_e + ^{40}\text{Ar} \rightarrow ^{40}\text{K}^* + e^-$

The first step in the analysis of solar neutrino events is the calculation of event and background rates.

### 4.1.1 Intensity of neutrino events

We consider separately neutrino elastic scattering (ES) on electrons and neutrino absorption by Argon with Fermi transition (F) to the 4.38 MeV Isotopic Analogue State (IAS) of  $^{40}\text{K}$ , and Gamow-Teller transitions (GT) to several  $^{40}\text{K}$  levels [24]. The  $^8\text{B}$  solar neutrino flux used in the calculation is taken from the BP98 standard solar model [25].

The elastic scattering event rate at different values of the cutoff kinetic energy of the recoil electron is computed by using the cross section values taken from Ref. [26]. For neutrino absorption, the shape of the cross section (evaluated for a transition to the IAS) is assumed to be the same for Fermi and Gamow-Teller transitions and the absolute values are computed by normalization to the theoretical values obtained by shell model calculations [24]. The Fermi and Gamow-Teller contributions to the neutrino absorption on  $^{40}\text{Ar}$  can also be obtained indirectly from measurements of the  $\beta^+$ -decay of the mirror nucleus  $^{40}\text{Ti}$ , assuming isospin symmetry. Two recent experiments have been performed. One of them [27], yields cross section values somewhat larger, while the second [28] essentially confirms the theoretical predictions. The lowest cross section values have been used for the present calculations.

The resulting neutrino interaction achievable with an exposure of 1 kton  $\times$  year, for ES, F and GT events, as a function of the threshold on the primary electron kinetic energy, are summarized in columns 2 to 4 of table 5.

### 4.1.2 Background estimates

The following background sources have been considered:

$T_{th}$ (MeV)	Events				
	Elastic	Fermi	Gamow-Teller	Photons	Neutrons
0.0000	2674	1964	1902	$1.40 \times 10^8$	15745
1.0000	2238	1928	1902	$3.83 \times 10^7$	7243
2.0000	1826	1792	1868	$2.14 \times 10^6$	3306
3.0000	1438	1530	1832		1481
4.0000	1092	1151	1702		677
5.0000	792	730	1453		306
5.5000		530	1094		
6.0000	540	355	694		140
6.5000		213	504		
7.0000	347	111	338		64
7.5000		47	204		
8.0000	204	15	106		28
8.5000		4	45		
9.0000	106		15		
9.5000			4		
10.000	49				

Table 5: Calculated solar neutrino reactions for an exposure of 1 kton  $\times$  year, as a function of the primary electron kinetic energy threshold  $T_{th}$ .

(a) *Natural radioactivity.*

The decay of  $^{40}\text{K}$ , uranium, thorium, radon and daughters, present in the rock or in the atmosphere surrounding the detector, generate photons and can produce neutrons by spontaneous fission (SF) or  $(\alpha, n)$  reactions.

(b) *Radioactive pollution in liquid Argon.*

There are two Argon isotopes which are radioactive, with long life times,  $^{42}\text{Ar}$  and  $^{39}\text{Ar}$ . While the  $^{39}\text{Ar}$  contamination is expected to be minimal,  $^{42}\text{Ar}$  is expected to be present in atmospheric Argon at the level of  $\leq 7 \times 10^{-22}$   $^{42}\text{Ar}$  atoms per natural Ar atom [29]. An experimental limit has been recently obtained of  $\leq 5 \times 10^{-21}$   $^{42}\text{Ar}$  atoms per natural Ar atom [30].

(c) *Radioactivity of structural materials.*

The materials constituting the dewar walls have been analyzed for radioactive contamination.

(d) *Nuclear photo-dissociation.*

In addition to the natural radioactivity, high energy cosmic ray muons which penetrate the rock, can induce nuclear photo-dissociation, with subsequent neutron production.

All these various contributions have been evaluated. Natural radioactivity of the rock turns out to be by far the most important background component and it is the only radiation source considered in our calculations. Particular care is devoted to neutrons, which are the only radiation able to generate high energy electrons in the energy range of the  $^8\text{B}$  neutrino spectrum.

The calculations of the background intensities are performed by detailed Monte Carlo simulations. The purpose of these computations is to derive the background event topology and the frequency and energy distribution of the resulting electron tracks in the sensitive volume, which can fake solar neutrino events.

The input background sources used in the Monte Carlo simulation are obtained from the measured photon [31] and neutron [32] spectra in the underground LNGS site. These were assumed to be a projection of the spectra of the particles emerging from the rock. The input neutron spectrum is the result of a direct measurement performed by the ICARUS collaboration in the Gran Sasso laboratory hall C. This measurement is in fairly good agreement with the result of a simulation considering the uranium and thorium specific activity of the LNGS rock [33]. Photons and neutrons are considered independently.

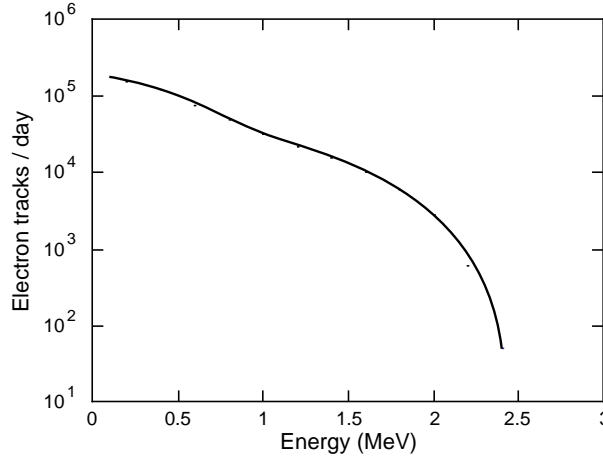


Figure 8: Integral electron track energy spectrum generated from photon interaction.

(a) *Photons.*

Photons penetrating in the detector undergo electromagnetic interactions, producing electrons in LAr. The energy distribution of these electron tracks in the detector is shown in figure 8. No electron tracks are expected with an energy larger than 2.4 MeV. Each event consists of a main track, possibly accompanied by electrons produced by the interaction of bremsstrahlung photons. The distribution of these events, according to the energy of the most energetic electron (primary track), is displayed in the fifth column of table 5.

(b) *Neutrons.*

Neutrons entering the detector may undergo neutron-capture followed by gamma ray emission. Gamma interactions produce electron tracks. The computation is performed in two steps. First, the calculation of the neutron capture intensity, occurring mostly in LAr, is performed by the MCNP code. The simulated ICARUS detector consists of an external neutron shielding layer, a thermal insulating material cavity, a liquid Argon dead region (0.35 m thick), and the inner sensitive volume. Second, the abundance of the events generated by the gamma rays and classified according to their nature (electron tracks multiplicity, energy, etc.) was calculated using a GEANT based simulation. The event topology after capture consists of a number of electron tracks produced by de-excitation or by bremsstrahlung photons. From this calculation about 15745 neutrino capture events

are expected for an exposure of  $1 \text{ kton} \times \text{year}$ . The distribution of these events, according to the energy of the most energetic electron track, is displayed in the last column of table 5.

The topologies of the neutron capture events, in which at least one electron has kinetic energy larger than 5 MeV (obtained with the GEANT program) are displayed in table 6 d). Here, the fraction of events is shown as a function of the Compton electron multiplicity and its associated energy (total energy of secondary electrons). This table, together with the values displayed in the last column of table 5, will allow the computation of the background contamination in each class of events.

## 4.2 Solar neutrinos detection

The choice of a primary electron kinetic energy threshold of 5 MeV, to select the solar neutrino event sample, is justified by statistical considerations on neutrino signal versus background event rates (reported in table 5). With this selection there is no photon background contribution, while a total sample of 2975 solar neutrino events is expected (for  $1 \text{ kton} \times \text{year}$  exposure), with a contamination of 306 events from neutron background.

In order to define off-line event versus background selection criteria, a full GEANT Monte Carlo simulation, which performs the transport of gamma rays and electrons inside the liquid Argon, has been carried out. Every electron track is then digitized by the following procedure:

- (a) The deposited energy is converted in charge.
- (b) The charge is drifted towards the anode of the chamber, with an infinite electron life time in LAr.
- (c) Digitized electronic signals are generated on three wire planes (forming the anode), placed at  $60^\circ$  from one another, with 3 mm wire pitch.
- (d) Gaussian distributed electronic noise is added with zero mean value and a RMS 1000 electrons. The resulting electron threshold, which is strongly correlated with electronic noise and with the sense wire pitch, is 150 keV.

The digitized signals are picked up from the noise by means of an integral-differential algorithm and the final parameters (position and energy after digitization) are obtained by a fitting procedure of the signals, equivalent to the procedures used for the analysis of real events.

As an example, a Monte Carlo absorption event is shown in figure 9. It is characterized by the track of the primary electron generated in the interaction, surrounded by a number of secondary tracks produced by photons following the  $^{40}\text{K}^*$  de-excitation.

The Monte Carlo simulation of ES and absorption events shows that the probability of finding secondary electron tracks vanishes 50 cm away from the interaction point. Electrons undergo strong multiple scattering and bremsstrahlung. Deviation from straight line tracks decreases with increasing energy (due to the  $1/p$  dependence showed by multiple scattering): track directions for electron energies larger than 5 MeV are efficiently reconstructed.

The correlation between Compton electron multiplicity and its associated energy will be used to define the off-line event selection criteria and to evaluate the selection efficiencies  $\epsilon_{ES}$ ,  $\epsilon_{GT}$  and  $\epsilon_F$  for scattering and absorption channels, and the background rejection power.

### 4.2.1 Elastic scattering

Electrons produced via an ES have an angular distribution, which is strongly peaked forward with respect to the initial solar neutrino direction, as shown in figure 10. This feature provides

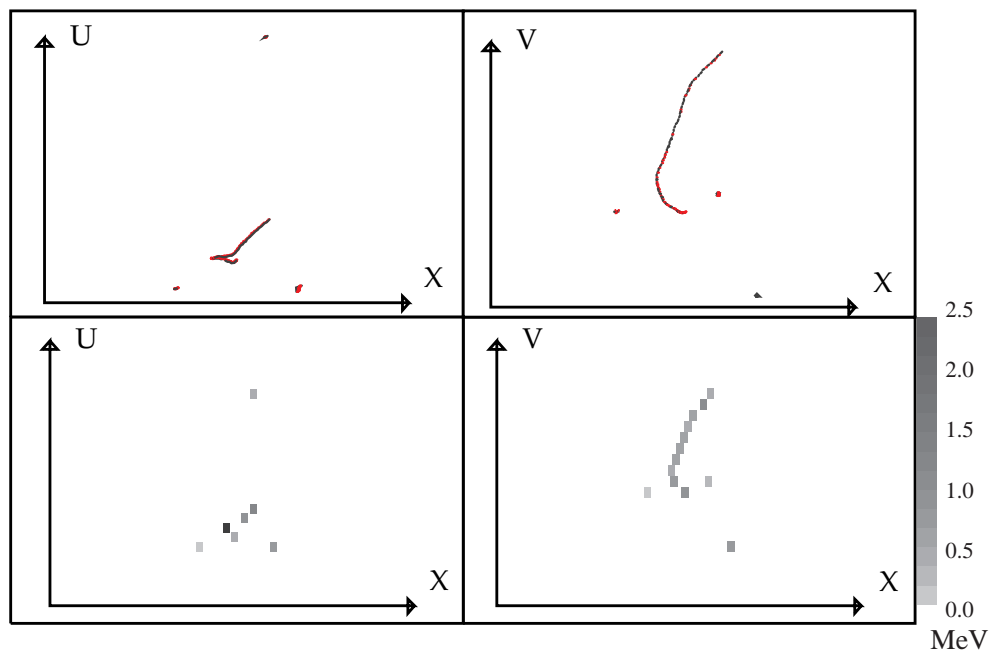


Figure 9: Top figure: an absorption event as simulated by the GEANT Monte Carlo program is shown in two wire planes (U and V coordinates) put at an angle of  $60^\circ$ , the X axis is the drift coordinate. The projected track length is about 3 cm, the main electron energy is 7 MeV, the associated energy is 2 MeV and the Compton electron multiplicity is 3. At the bottom the same event is shown after digitization and signal extraction. The grey scale of each pixel is proportional to the deposited charge. The resolution in the horizontal axis (drift direction) is 0.4 mm, and in the vertical axis is 3 mm (wire pitch).

an efficient mean to distinguish neutrino elastic events from background, assuming that the electron vertex is correctly reconstructed from the energy deposited along the track. In our computations the first hit wire can be distinguished from the end point of one electron with an efficiency larger than 80%. Moreover, electrons from ES reactions are essentially isolated. The fraction of the ES events as a function of the multiplicity and energy of the secondary tracks is shown in table 6 a).

a) Elastic scattering events				
Associated	Compton electron multiplicity			
Energy	0	1	2	3
$E < 1$ MeV	0.880	0.073	0.008	0
$E \geq 1$ MeV	0	0.015	0.015	0.009

b) Gamow-Teller events				
Associated	Compton electron multiplicity			
Energy	0	1	2	$\geq 3$
$E < 1$ MeV	0.083	0.168	0.049	0
$E \geq 1$ MeV	0	0.075	0.297	0.328

c) Fermi events				
Associated	Compton electron multiplicity			
Energy	0	1	2	$\geq 3$
$E < 1$ MeV	0.032	0.039	0.018	0
$E \geq 1$ MeV	0	0.081	0.221	0.519

d) Neutron capture events				
Associated	Compton electron multiplicity			
Energy	0	1	2	$> 2$
$E < 1$ MeV	0.46	0.26	0.10	0
$E \geq 1$ MeV	0	0.05	0.07	0.06

Table 6: Fraction of events with at least one electron with kinetic energy larger than 5 MeV, as a function of the Compton electron multiplicity and its associated energy. Data obtained after digitization are used.

Therefore, we assume the following off-line selection criteria for ES events:

1. primary electron energy larger than 5 MeV;
2. cone aperture around the direction of the emitted electron of  $25^\circ$ : efficiency  $\epsilon_1 = 0.65$ ;
3. Compton electron multiplicity  $M=0$ : efficiency  $\epsilon_2 = 0.88$ , see table 6 a).

The total detection efficiency is  $\epsilon_{ES} = 0.572$ , corresponding to an ES expected rate of 453 events, for 1 kton  $\times$  year exposure (see table 5).

The contamination of neutron capture events is 306 events (see table 5). Applying the ES selection criteria on the neutron sample (angular cut efficiency  $\epsilon_1 = 0.047$ , multiplicity cut  $\epsilon_2 = 0.46$ , using table 6 d)), we obtain 7 residual background events. If we are not able to determine the electron direction of flight, the angular cut efficiency is half and we remain with 14 background events.

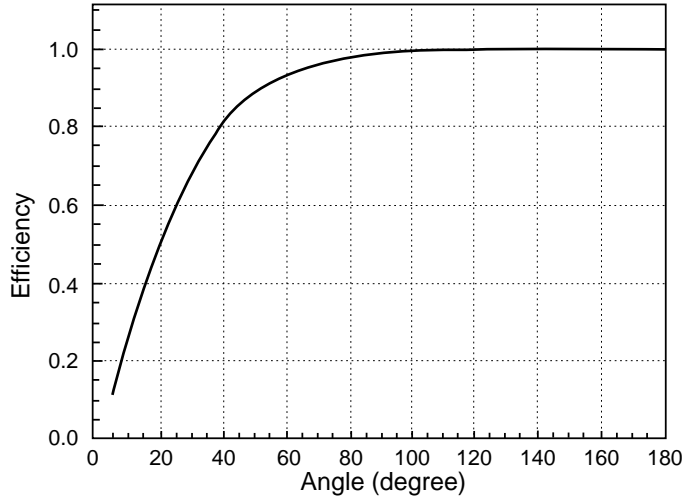


Figure 10: Fraction of elastic events ( $E > 5$  MeV) as a function of the cone angle within which the reconstructed electron direction in space is contained; the cone axis is defined by the parent neutrino direction. Three wire planes put at  $60^\circ$  angle and a 3 mm wire pitch are used.

#### 4.2.2 Absorption events

The angular distributions of electrons produced by absorption events, to a first approximation, can be considered isotropic, therefore angular cuts are not effective. Efficient discrimination criteria are based on associated energy and multiplicity cuts.

(a) *Allowed Gamow-Teller transitions.*

In table 6 b) the correlation between the associated multiplicity and secondary electron total energy for GT events is shown. We assume the following off-line selection criteria for the GT sample:

1. primary electron kinetic energy larger than 5 MeV;
2. associated energy  $E \geq 1$  MeV and multiplicity  $M \geq 1$ :  $\epsilon_{GT} = 0.70$ , see table 6 b).

The final expectation after cuts is 1017 events, for 1 kton  $\times$  year exposure.

(b) *Super allowed Fermi transition.*

In table 6 c) the correlation between the associated multiplicity and energy is shown.

We assume the following off-line selection criteria for F events:

1. primary electron kinetic energy larger than 5 MeV,
2. associated energy  $E \geq 1$  MeV and multiplicity  $M \geq 1$ :  $\epsilon_F = 0.82$ , see table 6 c).

The final expectation after cuts is 599 events, for 1 kton  $\times$  year exposure.

The total absorption rate (GT+F) is about 1616 events, for 1 kton  $\times$  year exposure, with a contamination from neutron captures of 55 events, applying the absorption cuts to the neutron sample (see table 5 and 6 d)).

Besides the neutron contamination, 8.3% of the GT and 3.2% of the F type events can fake an elastic scattering event, as can be seen in tables 6 b) and 6 c) (multiplicity  $M=0$ ). Taking

into account the angular cut, this reduces the contamination to 11 events, for 1 kton  $\times$  year exposure, in the ES sample. The contamination of the absorption sample from ES is 3.9%, i.e. 17 events, for 1 kton  $\times$  year exposure, as can be derived from tables 5 and 6 a) (multiplicity  $M \geq 1$  and associated energy  $\geq 1$  MeV).

### 4.3 Sensitivity to oscillations

We summarize the results in table 7, where the estimated rates of events per year are shown, together with the background rates. From this table we conclude that a clean measurement of  $^8\text{B}$  solar neutrinos can be performed in a reasonable data-taking time. Direct proof of the oscillation mechanism will be possible for a vast fraction of the presently allowed parameter region through the comparison of the elastic and absorption event rates (table 8). An accurate measurement of the  $^8\text{B}$  spectrum will also be performed by means of the absorption event sample. It is important to bear in mind that this is possible because of the low intensity of background signals. Noise is mainly related to the neutron flux level in the LNGS laboratories, but the radioactive contamination of the materials employed in the detector construction must be accurately considered. At present in one of the half-modules the electric-insulation material is not adequate from the point of view of the radiochemical purity. We estimate that this material will induce an increase of the background by a factor of 10. However, we plan to substitute it before the installation in the underground lab.

	Events/year
Elastic channel ( $E \geq 5$ MeV)	453
Background	14
Absorption event contamination	11
Absorption channels	1616
Background	55
Elastic event contamination	17

Table 7: Number of events expected with an exposure of 1 kton  $\times$  year, compared with the computed background (no oscillation).

In Super-K about 13 solar neutrino events/day (elastic scattering), with an energy threshold of 5 MeV, are observed. In the ICARUS T600 detector, with a neutrino oscillation hypothesis, 1.4 solar neutrino events/day (elastic scattering + absorption) with  $E > 5$  MeV are expected. Therefore, the statistical accuracy attainable with the T600 experiment is by far worse compared to Super-K. However, systematic uncertainty is expected to be lower, due to the higher event selection efficiency and energy resolution. More important, with ICARUS one can exploit the two available solar neutrino interaction processes. This is relevant to enhance the sensitivity to oscillation.

Recently the SNO experiment started operation (November 1999). The active mass is about 1 kton of heavy water ( $D_2O$ ) and the energy threshold is 5 MeV. The main solar neutrino detectable reactions are CC neutrino absorption by deuterium and NC neutrino dissociation of deuterium. In case of no oscillation, the two reactions follow the CC:NC=2.05:1.00 ratio. The expected number of CC reactions is about  $9 \times 10^3$  events/year, without taking into account efficiency cuts, depending on detector performance and varying with possible oscillation parameters [34]. At present (phase 1) only CC reactions can be detected, NC reaction detection will be possible in phase 2, when salt will be diluted in  $D_2O$ . Just as for radiochemical solar neutrino experiments, there is no energy discrimination for the NC reaction. Oscillation analysis



Solution region	$R$	Exclusion level	Minimal exposure (kton $\times$ year)
Active MSW - SMA	1.0 $\div$ 1.1	Nearly complete	2
Active MSW Extended SMA	1.1 $\div$ 1.3	Only the largest mixing side	$> 0.5$
Active MSW - LOW	1.1 $\div$ 1.3	Complete	$> 0.5$
Active MSW - LMA	1.3 $\div$ 1.9	Complete	0.5
Active MSW Extended LMA	1.2 $\div$ 2.3	Complete	0.5
Active JustSo	0.8 $\div$ 1.0	Partial	$> 0.5$
Active JustSo	1.0 $\div$ 2.0	Partial	$> 0.5$
Sterile MSW - SMA	0.8 $\div$ 0.9	Complete	0.5
Sterile MSW Extended SMA	0.6 $\div$ 0.8	All the higher mixing angle side	0.5
Sterile MSW Extended SMA	0.6 $\div$ 1.0	Complete	$> 0.5$

Table 8: The  $R$ -ratio range, the level of exclusion and the minimal exposure (units of 1 kton  $\times$  year).

is performed by the NC/CC ratio, i.e. with an approach similar to the one foreseen with ICARUS.

There is no doubt that the quality of the data and the extra measurements done with the T600 detector (i.e., with a different experimental technique) will be a major contribution to solar neutrinos understanding.

#### 4.4 Oscillation parameters allowed regions

A possible way to combine the ICARUS measurements from the two independent detection channels, elastic scattering and absorption events (Gamow-Teller and Fermi), is to compute the following ratio:

$$R = \frac{\frac{N^{ES}}{N_0^{ES}}}{\frac{1}{2} \left( \frac{N^{GT}}{N_0^{GT}} + \frac{N^F}{N_0^F} \right)} \quad (5)$$

where  $N^{ES}$ ,  $N^{GT}$ ,  $N^F$  are the measured event rates (elastic, Gamow-Teller and pure Fermi respectively), and  $N_0^{el}$ ,  $N_0^{GT}$ ,  $N_0^F$  are the predicted event rates in the case of standard neutrino without oscillations.

The proposed ratio is an indicator with the following advantages:

- it is independent of the  $^8\text{B}$  total neutrino flux, predicted by different solar models, and of any possible pure astrophysical suppression factor;
- it does not depend on experimental threshold energies or on the adopted cross-sections for the different channels.

The quantities introduced above are defined as follows.

$$N^{ES} = \Phi_{8B}^{SM} \int_{E_{\nu,\min}}^{+\infty} dE_{\nu} S(E_{\nu}) \left[ \sigma_{\nu_e}^{ES}(E_{\nu}) P(E_{\nu}) + \sigma_{\nu_{\mu(\tau)}}^{ES}(E_{\nu}) (1 - P(E_{\nu})) \right] \quad (6)$$

here  $E_{\nu}$  is the neutrino energy,  $S(E_{\nu})$  is the standard  $^8B$  neutrino spectrum,  $\sigma_{\nu_e}^{ES}(E_{\nu})$  is the elastic scattering cross-section for electron-neutrinos while  $\sigma_{\nu_{\mu(\tau)}}^{el}(E_{\nu})$  is the corresponding cross-section for mu-neutrinos or tau-neutrinos and  $P(E_{\nu})$  is the survival probability for  $\nu_e \rightarrow \nu_{\mu(\tau)}$  or  $\nu_e \rightarrow \nu_S$  transitions. In the second case the contribution has to be omitted. These probabilities are a function of neutrino parameters  $\Delta m^2$  and  $\sin^2 2\theta$ . The lower limit in the integral is

$$E_{\nu,\min} = \frac{1}{2} \left[ T_{th} + \sqrt{T_{th}^2 + 2T_{th}m_e} \right] \quad (7)$$

where  $T_{th}$  is the electron threshold kinetic energy and  $m_e$  is the electron mass.

For Gamow-Teller and Fermi transitions the corresponding event rates are defined as:

$$N^{GT} = \Phi_{8B}^{SM} \int_{E_{\nu,\min}^{GT}}^{+\infty} dE_{\nu} S(E_{\nu}) \sigma^{GT}(E_{\nu}) P(E_{\nu}) \quad (8)$$

where

$$E_{\nu,\min}^{GT} = T_{th} + 1.50 \text{ MeV} + 2.29 \text{ MeV}$$

and

$$N^F = \Phi_{8B}^{SM} \int_{E_{\nu,\min}^F}^{+\infty} dE_{\nu} S(E_{\nu}) \sigma^F(E_{\nu}) P(E_{\nu}) \quad (9)$$

where

$$E_{\nu,\min}^F = T_{th} + 1.50 \text{ MeV} + 4.38 \text{ MeV}.$$

The corresponding neutrino event rates without oscillation ( $N_0^{ES}$ ,  $N_0^{GT}$ ,  $N_0^F$ ) may be obtained from the previous formulae, putting  $P(E_{\nu}) \equiv 1$ .

The iso- $R$  curves for active neutrinos obtained from Monte Carlo simulation, taking into account neutrino oscillation, are shown in figure 11. The corresponding study for sterile neutrinos is reported in [23].

Shaded regions represent the allowed regions resulting from five solar neutrino experiments (Homestake-chlorine, Kamiokande, GALLEX, SAGE, and Super-Kamiokande) for 90% and 95% confidence level. The solutions of the SNP (which the ICARUS experiment will be able to probe) together with the  $R$ -ratio range, the level of exclusion, and the minimal exposure are reported in table 8.

There are combinations of neutrino parameters for which  $R = 1$ , despite of the fact that the MSW effect takes place in the sun. Such regions can not be excluded by this method and represent its theoretical limit. The experimental limit is given by the ICARUS ability to detect a small deviation from  $R = 1$ , which is related to the statistical error and all the experimental systematic error sources.

Taking into account only the statistical error and the rates reported above, we can estimate the one-sigma relative uncertainty for  $R$ , as a function of the exposure time. The results are given in table 9.

From the results above it is clear that it will be possible to test some of the currently allowed solutions with an exposure limited to 0.5-2 kton  $\times$  year.

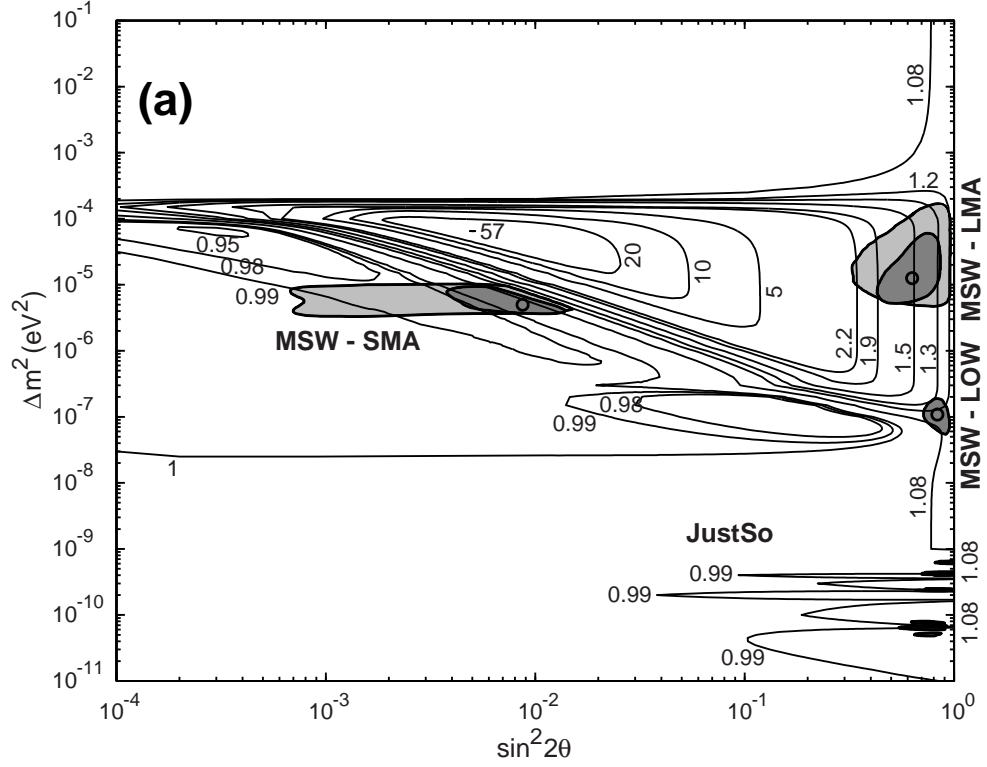


Figure 11: Iso- $R$  curves for active neutrinos.

Exposure (kton $\times$ year)	$\Delta R/R$ %	$R_{min}$	$R_{max}$
1	7.5	0.92	1.08
2	5.3	0.95	1.05
4	3.8	0.96	1.04

Table 9: One-sigma relative uncertainty for  $R$ , as a function of the exposure, and limits of the one-sigma exclusion region.

## 5 Nucleon decay searches

The question of baryonic matter stability is of paramount importance, since proton decay offers an unique way to have an insight of what happens beyond what currently appears to be the desert after the standard model. The theoretical ideas and models relevant to proton decay require some new, very high, intermediate mass scale. Such a mass scale will never be reached with today's acceleration techniques. Non-accelerator experiments are the only way to explore experimentally the phenomenology at such high energies.

The Super-Kamiokande collaboration has extensively probe the classical decay channels (e.g.,  $p \rightarrow e^+\pi^0$ ) and the dominant decay mode,  $p \rightarrow \bar{\nu}K^+$  according to SUSY Grand Unified Theories (see e.g. Ref. [35]). Plans exist to operate a megaton water Čerenkov detector [36] in view of improving current sensitivities for  $p \rightarrow e^+\pi^0$  and  $p \rightarrow \bar{\nu}K^+$  modes by at least one order of magnitude. However, to unmistakably show the existence of a signal, these experiments have to rely on statistical background subtraction.

A clear advantage and certainly the main strength of the ICARUS technique is, that discovery will be possible at the level of a single event, thanks to its superb imaging and energy resolution capabilities. In addition, a full understanding of the mechanism responsible for proton decay, requires a precise measurement of all possible branching ratios. Since ICARUS provides a much more powerful background rejection, it can perform a large variety of exclusive decay modes measurements. Inclusive searches are obviously also possible.

Hence, a liquid Argon detector is an ideal device, in particular, for those channels that are not accessible to Čerenkov detectors due to the complicated event topology, or because the emitted particles are below the Čerenkov threshold (e.g.  $K^\pm$ ). In particular, the operation of a T600 module, at the Gran Sasso laboratory, will be of the utmost importance to verify both, the predicted background levels and the anticipated detector efficiencies.

We have performed a detailed full event simulation based on the FLUKA package [8, 9] and the realistic events obtained contain very long tracks with redundant information, allowing particle identification and measurement of their energies with great precision. See, for instance, the spectacular example of the SUSY-preferred decay mode of the proton  $p \rightarrow \bar{\nu}K^+$  displayed in Figure 12. We can observe the increase in ionization deposition by the  $K^+$  as it comes to rest. There is no ambiguity in the direction of the particle along its trajectory. Particle identification benefits greatly from the ability to measure the ionization loss ( $dE/dx$ ). In particular, using  $dE/dx$  versus range only, an excellent separation is obtained between pions and kaons.

We report here the study for two specific channels:  $p \rightarrow e^+\pi^0$  and  $p \rightarrow \bar{\nu}K^+$  [37]. The estimation of backgrounds, due to atmospheric neutrino interactions, has been carried out using a statistical sample which is a thousand times larger than the one expected for a 1 kton  $\times$  year exposure.

### 5.1 $p \rightarrow e^+\pi^0$ decay mode

This is one of the mode favored by minimal SU(5) theories. The list of cuts used for the exclusive scenario search is presented in table 10, normalized to an exposure of 1 kton  $\times$  year. In the presence of nuclear matter, pion induced reactions are complex, mainly because of two and three nucleon absorption processes. Pion-nucleon interactions can proceed through the non-resonant and the p-wave channels with the formation of a  $\Delta$  resonance. The  $\Delta$  can either decay (resulting in elastic scattering or charge exchange), or interact with surrounding nucleons, resulting in pion absorption. In s-wave absorption, the relative probability of absorption on a np pair or on a nn or pp pair, is assumed to be the same as in p-wave absorption. Our nuclear interaction generator [8, 9] foresees that  $\sim 45\%$  of the times the  $\pi^0$  is absorbed and therefore not visible.

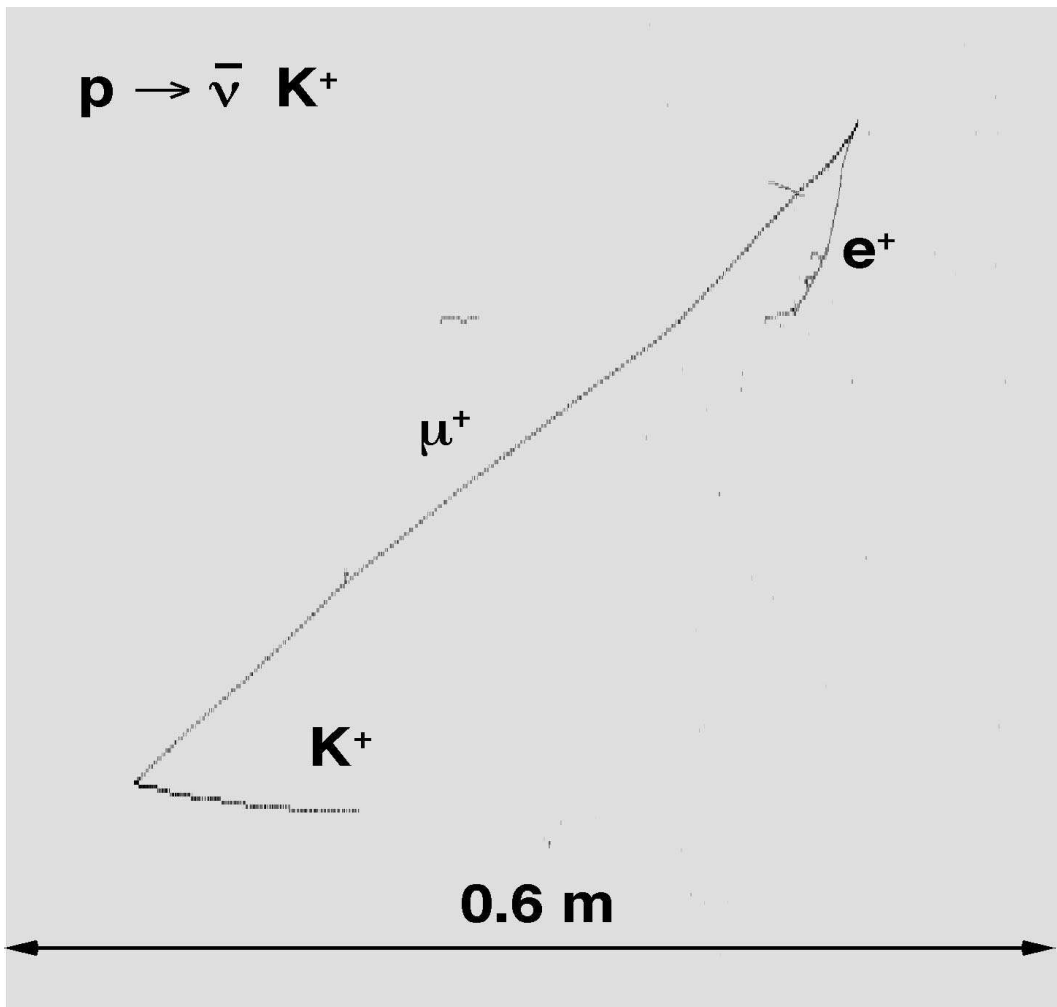


Figure 12: Simulated proton decay in the preferred channel in Supersymmetric models  $p \rightarrow \bar{\nu} K^+$  as could be observed in ICARUS .

The idea behind the kinematic cuts is to have a balanced event, with all particles identified, and with a total invariant mass compatible with that of a proton.

<b>Exclusive Channel Cuts</b>	$p \rightarrow e^+\pi^0$	$\nu_e$ CC	$\bar{\nu}_e$ CC	$\nu_\mu$ CC	$\bar{\nu}_\mu$ CC	$\nu$ NC
One $\pi^0$	54%	6.6	2.1	15	5.8	11.1
One electron	54%	6.6	2.1	0.02	0	0
$E_{proton}^{kinetic} < 100$ MeV	52%	2.7	1.4	0.004	0	0
$0.93 < E_{total} < 0.97$ GeV	38%	0.03	0.01	0	0	0
$P_{total} < 0.46$ GeV	37%	0	0	0	0	0

Table 10: Cuts for the  $p \rightarrow e^+\pi^0$  channel. Survival fraction of signal (first column) and background events through event selections applied in succession (normalized to an exposure of 1 kton  $\times$  year).

After asking for one electron, only the  $\nu_e$  CC and  $\bar{\nu}_e$  CC backgrounds survive. The key cut is the total visible energy. A cut on the total visible energy is actually more efficient rejecting background than a cut on the invariant mass. No background events are expected for an overall predicted efficiency of about 37%.

## 5.2 $p \rightarrow \bar{\nu}K^+$ decay mode

This is one of the favored SUSY decays, and is special because of the presence of a strange meson in the final state. The conservation of strangeness leads to very different interactions of the  $K^+$ ,  $K^0$  and  $K^-$ ,  $\bar{K}^0$  with nucleons at low energies.  $K^-$  have a large cross section for hyperon production, with the  $\Sigma\pi$  and  $\Lambda\pi$  channels always open. They feel, like pions, a strong nuclear potential, and therefore are strongly absorbed by nuclei. On the other hand,  $K^+$  interact relatively weakly, therefore the fraction of positive kaons absorbed by nuclei is at the level of a few per cent.

ICARUS profits from its very good particle identification capabilities to tag the kaon and its decay products. Applying the cuts listed in table 11, a very good efficiency of 97% is reached for a negligible background. One topological cut (ask for the presence of only one kaon in the event) and one kinematic cut on the total energy are sufficient to obtain the quoted result.

<b>Cuts</b>	$p \rightarrow \bar{\nu}K^+$	$\nu_e$ CC	$\bar{\nu}_e$ CC	$\nu_\mu$ CC	$\bar{\nu}_\mu$ CC	$\nu$ NC	$\bar{\nu}$ NC
One Kaon	97%	0.310	0.059	0.921	0.214	0.370	0.104
No $\pi^0$	97%	0.161	0.030	0.462	0.107	0.197	0.051
No electrons	97%	0	0	0.455	0.107	0.197	0.051
No muons	97%	0	0	0	0	0.197	0.051
No charged pions	97%	0	0	0	0	0.109	0.022
$E_{total} < 0.8$ GeV	97%	0	0	0	0	0	0

Table 11: Cuts for the  $p \rightarrow \bar{\nu}K^+$  channel. Survival fraction of signal (first column) and background events through event selections applied in succession (normalized to an exposure of 1 kton  $\times$  year).

## 5.3 Sensitivity to nucleon decay

To calculate partial lifetime lower limits,  $(\tau/B)$ , we use the following formulae:

$$(\tau/B)_p > \frac{2.69}{S} \times Expo \times \epsilon \times 10^{32} \text{ yrs} \quad (\text{proton decay})$$

$$(\tau/B)_n > \frac{3.29}{S} \times Expo \times \epsilon \times 10^{32} \text{ yrs} \quad (\text{neutron decay})$$

Here,  $Expo$  is the full detector exposure in kilotons per year,  $\epsilon$  is the selection efficiency, and  $S$  is the constrained 90% CL upper limit on the number of observed signal events.

$S$  is found by solving the equation:

$$\frac{\sum_{n=0}^{n_0} P(n, b + S)}{\sum_{n=0}^{n_0} P(n, b)} = \alpha$$

where  $P(n, \mu)$  is the Poisson function,  $e^{-\mu} \mu^n / n!$ ,  $b$  is the estimated background,  $\alpha = 0.1$  for a 90% CL, and, since we are computing the “detector sensitivity”,  $n_0$  is equal to the closest integer number to  $b$ .

For each nucleon decay channel we have computed the  $(\tau/B)$  limits as a function of the exposure. The detection signal efficiency ( $\epsilon$ ) and the expected background at each exposure is used to compute the corresponding upper limit ( $S$ ).

The top (bottom) part of figure 13 shows the predictions on the number of background events as a function of the exposure, for the proton (neutron) decay channels. The tables on the corner of each plot give the values at 1 kton×year. As expected, the exclusive channels have much less background than the inclusive ones. The gap between the two groups (a factor  $\sim 10^2$ ) can be clearly seen in the figure (compare for instance  $p \rightarrow e^+ \pi^+ (\pi^-)$  and  $p \rightarrow e^+ \pi^+ \pi^-$ ).

From an experimental point of view, this result has two important consequences. First of all, we observe that there are channels with a moderate expected contamination already at exposures of  $\sim 1$  kton×year. Clearly, the operation of a T600 module, at the Gran Sasso laboratory, will be of paramount importance to verify the detector efficiencies. On the other hand, we find channels that are almost background free up to exposures of 1 megaton×year. This confirms ICARUS strength to detect proton decay at the one-event level.

The obtained proton (neutron) limits on  $(\tau/B)$  as a function of the exposure are illustrated on the top (bottom) part of figure 14. The tables on the plots indicate the signal efficiencies and the estimated number of background events for an exposure of 1 kton×year. In general, the better limits are obtained on the exclusive channels. The tag based on the presence of a kaon or a pion accompanied by a charged lepton, with total measured energy around the proton mass, is powerful enough to annihilate the background.

Finally, we have studied how the previous limits on  $(\tau/B)$  compare with the current PDG limits [20]. Figure 15 shows what would be the minimum exposure needed to reach the present PDG limits on the different proton (top) and neutron (bottom) decay modes. Both, the used PDG values and the obtained exposures, are listed on the plots. It is important to remark that the limits reported in the PDG refer only to the exclusive channels, so the comparison shown in figure 15 is only strictly correct for these channels. Nevertheless, we also found it interesting to

show, how the ICARUS inclusive limits compare with the PDG exclusive ones. The modest mass provided by a T600 module is clearly insufficient to improve existing limits for a vast majority of the reported decay channels. However, we observe that two years of running will suffice to increase the sensitivity in channels like, for example,  $p \rightarrow \pi^+ \bar{\nu}$  and  $n \rightarrow e^- K^+$ .

The Super-Kamiokande collaboration has recently presented preliminary results coming from  $70 \text{ kt} \times \text{year}$  detector exposure [35]. In particular for the  $p \rightarrow e^+ \pi^0$  mode the proton lifetime has been found to be higher than  $4.4 \times 10^{33}$  years, while for  $p \rightarrow \bar{\nu} K^+$  the new bound is  $1.9 \times 10^{33}$  years at 90% c.l. The current results show that while a background-free search can be extended for modes like  $p \rightarrow e^+ \pi^0$  and  $p \rightarrow \mu^+ \pi^0$ , non-zero background is already expected for the  $p \rightarrow \nu K^+$  search. In a water Cherenkov detector the kaon is below threshold for light emission and low-background signatures can be obtained only at the expense of low efficiency cuts. In particular detection of low-energy gamma rays (6.3 MeV) is crucial to background reduction for this mode. This requirement calls for a large photo-cathode coverage in a future detector based on this technique. Thus only a third of the planned half a megaton UNO detector [36] is going to be dedicated for  $p \rightarrow \bar{\nu} K^+$  search. Consequently a potential for sensitivity improvement for the most favored SUSY modes is limited with water Cherenkov technique and a liquid argon detector may provide a unique opportunity to either discover a nucleon decay signal or to rule out a large class of theoretical models [38, 39].

## 6 Supernova neutrinos

### 6.1 Characteristics of a supernova collapse

For the first few seconds, the gravitational core collapse of a single star emits an intense burst of neutrinos whose luminosity rivals the total optical emissions of the observable universe. The detection of 20  $\bar{\nu}_e$  events from SN1987A (12 in Kamiokande [40] and 8 in IMB [41]) most economically constrained the properties of neutrino mixing, neutrino masses, neutrino magnetic moment, neutrino decay, etc. Those 20 events, however, could not identify any of the dynamical characteristics of the supernova mechanism that are stamped up in its neutrino signatures: shock break-out, convection, accretion, explosion, core cooling, and transparency. Nor was it possible that any  $\nu_\mu$  or  $\nu_\tau$  be detected, despite the prediction that these neutrino species and their anti-particles carry away the bulk of the neutron star binding energy.

Since then, new experiments have started taking data. For example, the collection of hundreds to thousands of events is anticipated by the dedicated LVD experiment. Such information will resolve the many outstanding questions in supernova modeling, as well as measure or constrain the properties of all three generations of neutrinos more tightly than can now be done in a laboratory. The contribution of ICARUS can provide pieces of the puzzle not duplicated by other experiments.

In order to examine the response of ICARUS to a supernova collapse in our Local Group of galaxies, we employ here a generic but detailed model of neutrino emission that reflects the latest calculations in Type II supernova theory. This baseline model of luminosities and spectra for each of the neutrino species incorporates various generic features of the dynamics of stellar collapse, but is not tied to any particular model. This patchwork model has been presented in Ref. [42] specifically for the purpose of studying and comparing the response and sensitivity of various neutrino detectors. In Figure 16 we reproduce from Ref. [42] the structure of the  $\nu_e$ ,  $\bar{\nu}_e$ , and “ $\nu_\mu$ ” luminosity curves for the first second of emission, where “ $\nu_\mu$ ” denotes the muon and tau neutrinos and their antiparticles collectively; Figure 17 shows the same for the first 50 seconds. The total energy radiated by this model is  $3 \times 10^{53} \text{ erg}$ , which corresponds to  $2.8 \times 10^{57} \nu_e$ ,



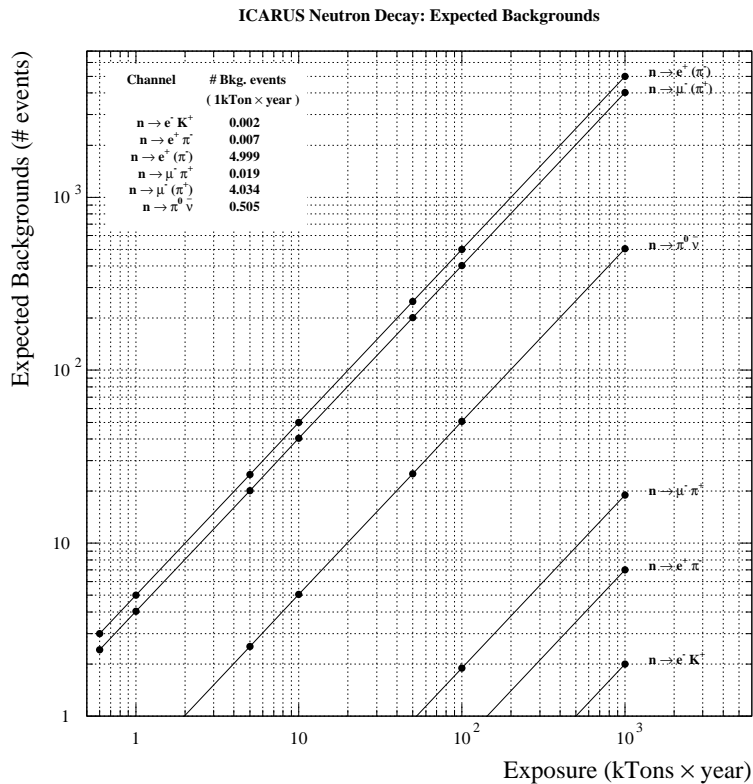
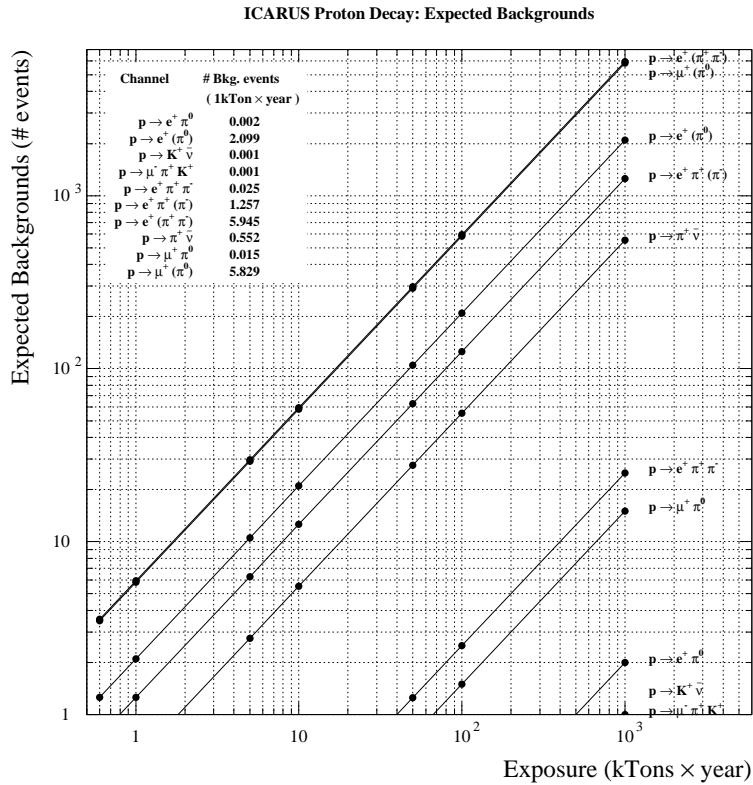


Figure 13: Estimated number of background events as a function of the exposure for the different proton (top) and neutron (bottom) decay channels. The tables in the plots give the precise values for an exposure of 1 kton×year.

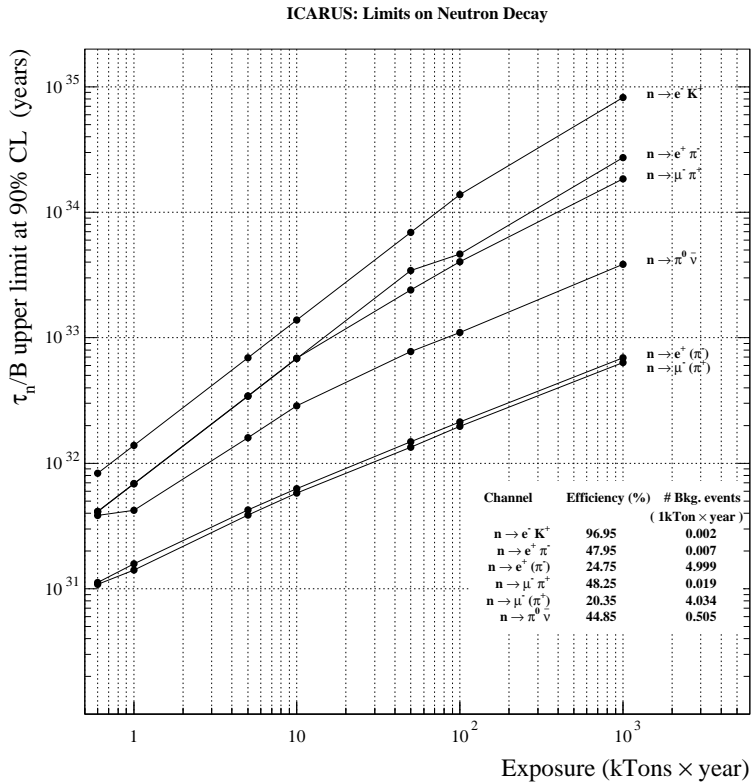
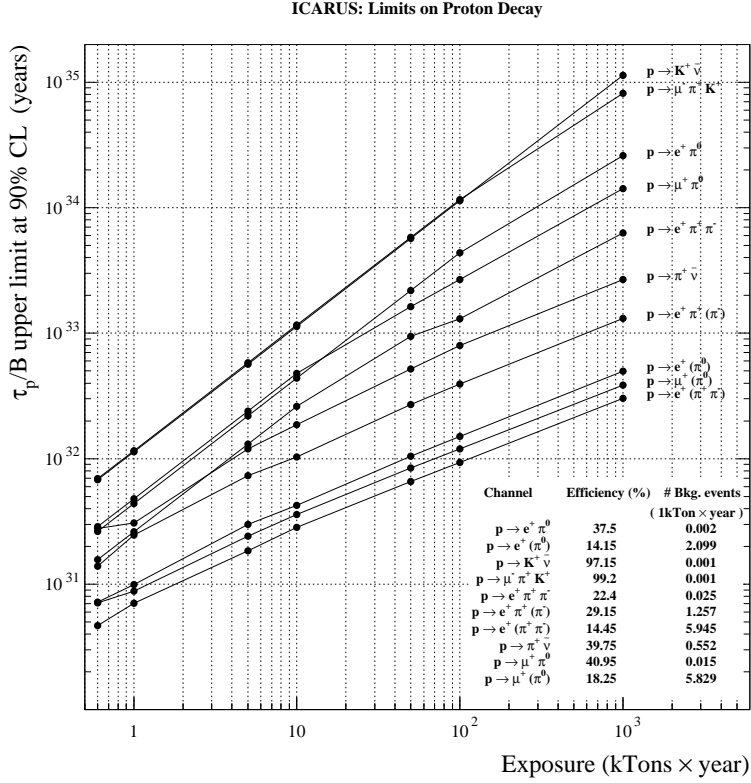


Figure 14: Running of the proton (top) and neutron (bottom) decay lifetime limits ( $\tau/B$ ) with the exposure. The limits are at 90% confidence level. The tables indicate the selection efficiencies and the estimated number of background events for each decay mode, at an exposure of 1 kton $\times$ year.

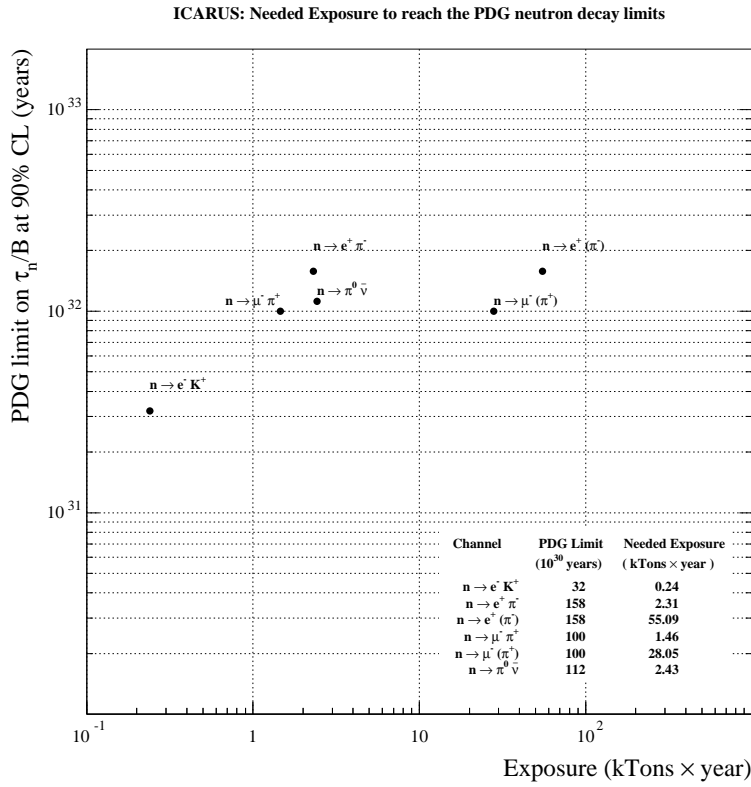
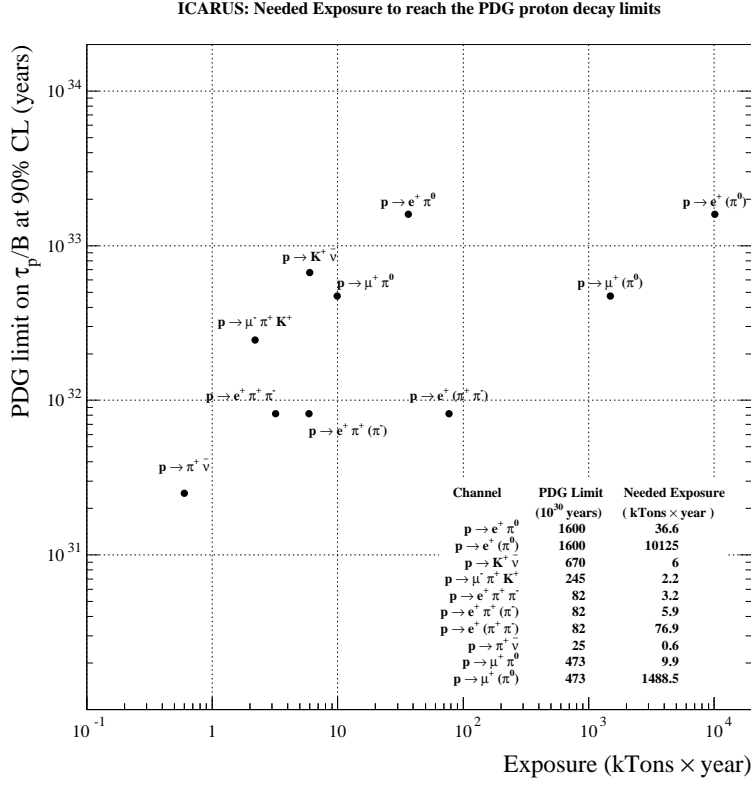


Figure 15: Needed exposure (in kilotons $\times$ year) to reach the current PDG proton (top) and neutron (bottom) decay limits. The tables indicate, for each decay mode, the precise values of the PDG limits used and the obtained values of the needed exposure.

$1.9 \times 10^{57} \bar{\nu}_e$  and  $4.9 \times 10^{57} \nu_{\mu,\tau} + \bar{\nu}_{\mu,\tau}$  for a total of  $9.6 \times 10^{57}$  neutrinos. The integrated average energies are 11 MeV, 16 MeV, and 25 MeV, respectively.

## 6.2 The neutrino signal

From Figures 16 and 17 it is clear that the neutrino emissions are rich in diagnostic features of core collapse dynamics and neutron star formation. Here we list some of the main features only, for the purpose of their identification in the detected neutrino signals. Details may be found in the abundant literature; see, for example, Refs.[43, 44, 45, 46]. In Figure 16 the  $\nu_e$  ramp at times less than zero is indicative of the accelerating rate of electron capture in the collapsing core. The rebound of the inner core into the supersonic outer core creates a strong shock wave ( $t = 0$ ), accompanied by the  $\nu_e$  neutronization burst (the spike of Figure 16), and the sudden turn-on of the  $\bar{\nu}_e$  and “ $\nu_\mu$ ” radiation.

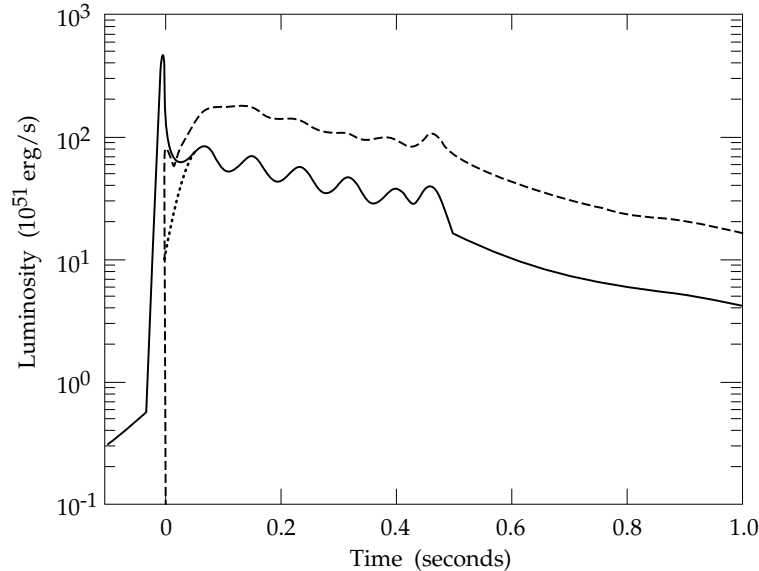


Figure 16: Luminosity curves for  $\nu_e$  (solid),  $\bar{\nu}_e$  (dots), and “ $\nu_\mu$ ” (dashes) for the first second of emission.

Immediately after the burst, the  $\nu_e$  spectrum makes a sudden transition to a more thermal distribution, with an average energy of about 10 MeV. The  $\bar{\nu}_e$  spectrum is harder, with an average energy of 16 MeV. Since the muon and tau neutrinos and their antiparticles interact at these temperatures only via neutral current interactions, their neutrinosphere lies somewhat deeper within the core. Their spectra is therefore hotter than either the  $\nu_e$  or  $\bar{\nu}_e$  spectra, about 25 MeV. Within 20 ms of bounce, hydrostatic equilibrium is achieved and a protoneutron star is formed; the  $\nu_e$  and  $\bar{\nu}_e$  luminosities now merge. At this stage the protoneutron star is fattened by accretion of the outer core matter. Either the shock wave continues into the outer stellar envelope or it stalls, only to be revived within hundreds of milliseconds or seconds by neutrinos from the core; these are the so-called prompt and delayed mechanisms, respectively, of core collapse. In this patchwork model, the bounce shock fizzles into an accretion shock, and subsequent neutrino heating of the shocked envelope re-energizes the shock into a supernova at 450 ms.

Oscillations in the mass accretion rate modulate the neutrino luminosities, as indicated in Figure 16, between 30 and 420 ms. At 450 ms the explosion which causes the ejection of the outer envelope and the optical supernova display occurs. Accretion shock may delay the

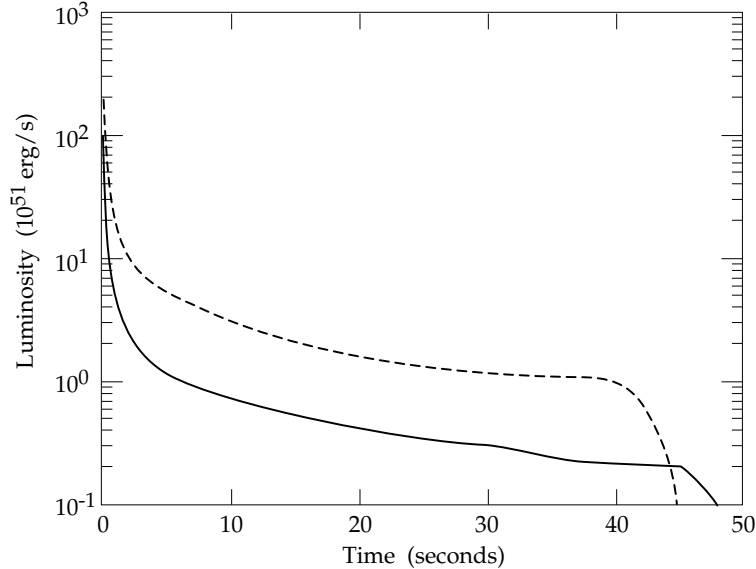


Figure 17: Luminosity curves for  $\nu_e$  (solid),  $\bar{\nu}_e$  (dots), and “ $\nu_\mu$ ” (dashes) for the first 50 seconds of emission.

explosion by 0.5 seconds to some several seconds; its inclusion here serves to display a possible structure of neutrino emission, rather than being a necessary prediction of the Standard Model. Quick spectral hardening, on the other hand, is predicted to accompany explosion whether it is prompt or delayed. While the first 100 ms are rich in diagnostic structure, the protoneutron star then begins a long cooling phase which may account for most of the energy emitted. During cooling the neutrino luminosities decay smoothly according to power laws which reflect the nonlinearity of neutrino transport. The long duration is a consequence of the high densities and high neutrino energies, which imply high opacities in the protoneutron star interior. It is expected that the thousands of events detected from such a collapse be spread over many tens of seconds to a minute or more, but that as the neutrino energies soften a larger fraction of the emitted luminosity will be shunted below detector thresholds. Finally, the cooling phase ends when the core becomes transparent to neutrinos and the luminosities plummet ( $t = 46$  and  $42$  s in the model used here for  $\nu_e(\bar{\nu}_e)$  and “ $\nu_\mu$ ” respectively). Again, since the “ $\nu_\mu$ ” opacities are lower than the  $\nu_e$  and  $\bar{\nu}_e$  opacities, it is predicted that the “ $\nu_\mu$ ” emissions should fall off first.

### 6.3 Event rate in the ICARUS detector

Models of type II supernovae predict that neutrinos are emitted with a thermal spectrum, with a temperature hierarchy among neutrino flavors:  $T_{\nu_e} < T_{\bar{\nu}_e} < T_{\nu_\mu, \nu_\tau, \bar{\nu}_\mu, \bar{\nu}_\tau}$ . The neutrino energy spectra can be described by a Fermi-Dirac distribution [47]:

$$\frac{dN}{dE_\nu} = \frac{C}{T^3} \frac{E_\nu^2}{1 + e^{(E_\nu/T - \eta)}} N_\nu \quad (10)$$

where  $C = 0.55$ ;  $T$  is the temperature (MeV);  $E_\nu$  the neutrino energy (MeV);  $\eta$  the chemical potential and  $N_\nu$  the number of expected neutrinos of a given species. We assume  $\eta = 0$  [47]. The following values for the different neutrino temperatures and average energies are used:

$$\begin{aligned}
\nu_e \quad T = 3.5 \text{ MeV} &\Rightarrow \langle E \rangle = 11 \text{ MeV} \\
\bar{\nu}_e \quad T = 5.0 \text{ MeV} &\Rightarrow \langle E \rangle = 16 \text{ MeV} \\
\nu_{\mu,\tau} \quad T = 8.0 \text{ MeV} &\Rightarrow \langle E \rangle = 25 \text{ MeV} \\
\bar{\nu}_{\mu,\tau} \quad T = 8.0 \text{ MeV} &\Rightarrow \langle E \rangle = 25 \text{ MeV}
\end{aligned}$$

We assume the supernova occurs at 10 kpc, a distance which includes 53% of the stars in the galactic disk [48]. All stars in the Milky Way lie within 30 kpc of the Earth. To calculate the theoretical count rates for this particular supernova in the ICARUS detector, we convolute the luminosities of the various  $\nu$  species as a function of time (Figure 17) with the neutrino scattering and absorption cross-sections on liquid Argon and with the average energy spectra as a function of time.

In ICARUS two reactions contribute to the total rate:

- **Elastic scattering:**  $\nu_x + e^- \rightarrow \nu_x + e^-$  ( $x = e, \mu, \tau$ ) sensitive to all neutrino species.
- **Absorption:**  $\nu_e + {}^{40}\text{Ar} \rightarrow e^- + {}^{40}\text{K}^*$ , (super-allowed Fermi and Gamow-Teller (GT) transitions [24] are possible).

The elastic neutrino scattering off electrons has a total cross section that increases linearly with energy:

$$\begin{aligned}
\sigma(\nu_e e^- \rightarrow \nu_e e^-) &= 9.20 \times 10^{-45} E_{\nu_e} (\text{MeV}) \text{ cm}^2 \\
\sigma(\bar{\nu}_e e^- \rightarrow \bar{\nu}_e e^-) &= 3.83 \times 10^{-45} E_{\bar{\nu}_e} (\text{MeV}) \text{ cm}^2 \\
\sigma(\nu_{\mu,\tau} e^- \rightarrow \nu_{\mu,\tau} e^-) &= 1.57 \times 10^{-45} E_{\nu_{\mu,\tau}} (\text{MeV}) \text{ cm}^2 \\
\sigma(\bar{\nu}_{\mu,\tau} e^- \rightarrow \bar{\nu}_{\mu,\tau} e^-) &= 1.29 \times 10^{-45} E_{\bar{\nu}_{\mu,\tau}} (\text{MeV}) \text{ cm}^2
\end{aligned} \tag{11}$$

All neutrino species contribute to elastic scattering. The experimental signature consists of a single recoil electron. Since, the direction of this electron is highly correlated to the incoming  $\nu$  direction, these events have the potentiality of precisely determining the location of the supernova source.

Reaction	T (MeV)	$\langle E_\nu \rangle$ (MeV)	Expected events	
			0.6 ktons	1.2 ktons
<b>Elastic</b>				
$\nu_e e$	3.5	11	4	8
$\bar{\nu}_e e$	5	16	2	4
$(\nu_\mu + \nu_\tau) e$	8	25	1	2
$(\bar{\nu}_\mu + \bar{\nu}_\tau) e$	8	25	1	2
total $\nu e$			8	16
<b>Absorption</b>				
$\nu_e \text{Ar}$ (Fermi)	3.5	11	15	30
$\nu_e \text{Ar}$ (GT)	3.5	11	30	60
<b>Total</b>			53	106

Table 12: Expected neutrino rates for a supernova at a distance of 10 kpc, releasing  $3 \times 10^{53}$  ergs of binding energy. No energy threshold for electron detection has been applied.

Table 12 shows the expected rates for this reaction. To compute the number of events we fold the total cross section as a function of energy with the appropriate Fermi-Dirac distribution. Our rates are calculated integrating over all electron recoil energies. Since the neutrino burst occurs in a time window of about 10 seconds, we estimate that the background expected due

Supernova neutrino rates in 600 TON ICARUS

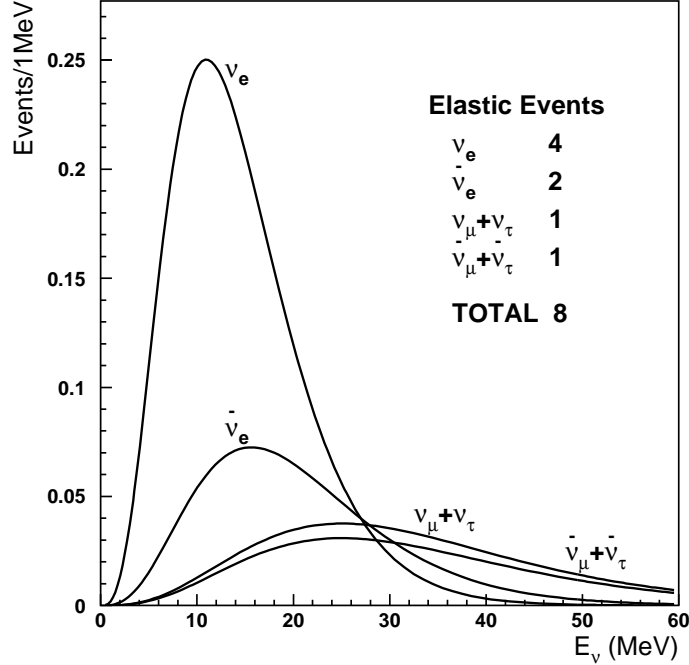


Figure 18: Expected elastic neutrino rates for a type II supernova at a distance of 10 kpc. Rates are integrated over all possible electron energies.

to natural radioactivity is negligible and therefore we do not apply any detection threshold for electrons.

Figure 18 shows the expected elastic event rates, as a function of the incoming neutrino energy, for the case of a 600 tons detector and a supernova occurring at 10 kpc. The largest contribution ( $\sim 50\%$ ) to elastic events comes from  $\nu_e$ , since they have both the larger flux and cross section. For a 0.6 (1.2) kton detector, we expect a total of 8 (16) elastic events.

The absorption rate is expected to proceed through two main channels: a superallowed Fermi transition to the 4.38 MeV excited isobaric analog  $K^*$  state; Gamow-Teller transitions to several excited K states. The two processes can be distinguished by the energy and multiplicity of the  $\gamma$  rays emitted in the de-excitation and by the energy spectrum of the primary electron.

The cross section for the Fermi  $\nu_e$  capture is given by [49]:

$$\sigma = 1.702 \times 10^{-44} E_e \sqrt{E_e^2 - m_e^2} F(E_e) \text{ cm}^2 \quad (12)$$

where the Fermi function,  $F(E_e)$ , has a value of 1.56 for electron energies above 0.5 MeV. The prompt electron energy is  $E_e = E_\nu + Q - m_e$ ;  $Q$  is the energy threshold ( $Q = 5.885$  MeV) and  $m_e$  is the electron mass. We consider that the GT transition has a cross section which is a factor two larger than the one quoted for Fermi absorption [24].

The absorption cross section is larger than for neutrino electron elastic scattering, hence this process significantly enhances the sensitivity of ICARUS as a supernova neutrino detector. Table 12 shows the expected rates in case of  $\nu_e$  absorption in Ar. In a 0.6 (1.2) kton detector, we expect around 45 (90) absorption events from a supernova located at 10 kpc from Earth.

Figures 19 and 20 show the total rate for a 0.6 and 1.2 kton detector as a function of supernova distance. It also displays the expected rates for the different neutrino reactions. For

a gravitational stellar collapse occurring in the Large Magellanic Cloud (distance  $\sim 60$  kpc), we expect to collect, in a 0.6 (1.2) kton detector, 2 (4) events as a result of the neutrino burst.

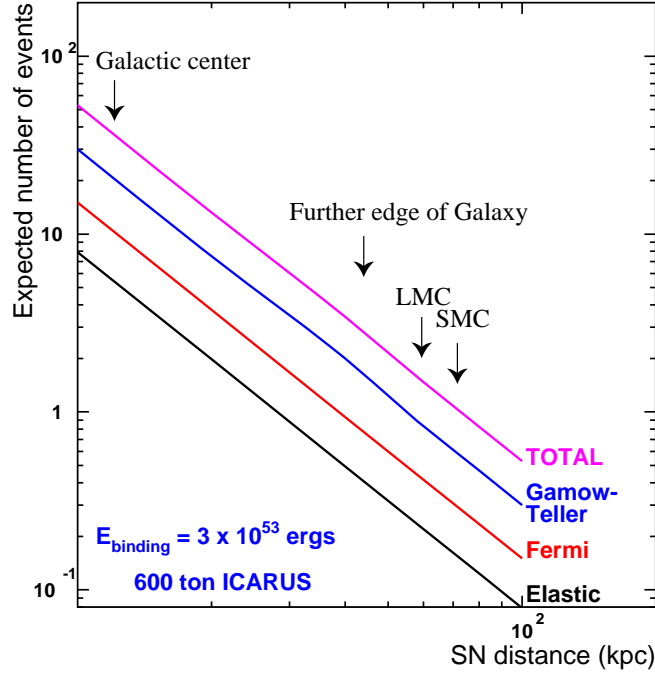


Figure 19: Predicted number of neutrino events for elastic and absorption reactions as a function of the supernova distance. We consider a 600 ton detector.

The rich event yield of the first second allows many of the characteristics of the supernova mechanism to stand out clearly: the  $\nu_e$  neutronization burst, the rapid turn-on of the  $\bar{\nu}_e$  and “ $\nu_\mu$ ” radiation, the accretion shock oscillations, the explosion pulse, and the long cooling of the core. The  $\nu_e$  burst is of particular interest and the sensitivity of ICARUS to this feature is paralleled only by LVD and SNO; the light-water detectors, such as IMB and Kamiokande II, did not have sufficient  $\nu_e$  sensitivity to detect it. The count rate peaks at 1200 Hz (but lasts only about 20 ms).

While special triggering will be necessary for readout of such a fast event rate, no problems are expected with data acquisition as ICARUS has effectively no dead time. Accretion shock modulation of the  $\nu_e$  luminosity, depending on its amplitude and period of oscillation, may also be discernible by bunching, or pulses of about 5 events. The explosion peak should be easily detected, as well as the gradual drop in count rate, on account of ICARUS’s low energy threshold. The overall electron scattering rate in ICARUS, when compared with the event rate of  $\nu_e$  absorption, will provide one of the first direct confirmations of the existence of the  $\nu_\mu$  and  $\nu_\tau$  components in the supernova emission. The light-water neutrino detectors, on the other hand, are largely insensitive to these neutrino species. Another advantage of the neutral-current sensitivity of ICARUS is the fact that the forward-peaked electron scattering events will point back to the direction of the supernova, thus providing confirmation of their origin.

The time structure of the luminosity of the next detected stellar collapse, and the absence or presence of structure within it, will yield a wealth of information on the explosion mechanism as well as on neutrino properties. ICARUS may contribute with hundreds of events to the total



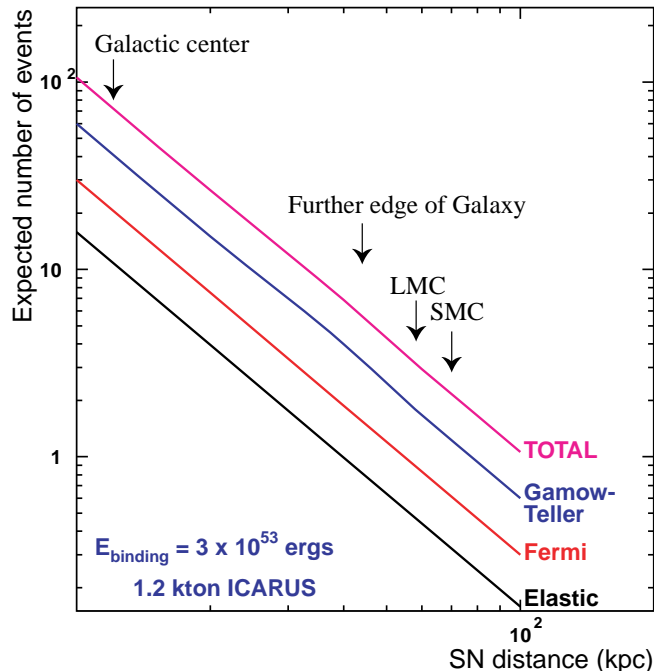


Figure 20: Predicted number of neutrino events for elastic and absorption reactions as a function of the supernova distance. We consider a 1.2 kton detector.

sample of thousands that will be collected by the international effort. ICARUS's neutral-current sensitivity will render a part of its contribution complementary to those of other detectors. On account of the good energy and angle resolution of the detector, its accurate timing, and effectively zero dead time, these events will be rich in information on the energy, timing, angle, and flavour content of the explosion. Of particular consequence is the fact that ICARUS can be expected to be sensitive to the initial  $\nu_e$  neutronization burst, important for the study of effects of a finite neutrino mass, as well as the  $\nu_\mu$  and  $\nu_\tau$  components in the supernova emission.

## References

- [1] ICARUS Collab., 'ICARUS-II. A Second-Generation Proton Decay Experiment and Neutrino Observatory at the Gran Sasso Laboratory', Proposal Vol. I & II, LNGS-94/99, 1994.
- [2] Y. Fukuda *et al.* [Super-Kamiokande Collaboration], Phys. Rev. Lett. **81**, 1562 (1998), hep-ex/9807003.
- [3] ICARUS Collab. "A first 600 ton ICARUS Detector Installed at the Gran Sasso Laboratory", Addendum to proposal, **LNGS-95/10** (1995).
- [4] T. Gaisser (*Cosmic Rays and Particle Physics*) Cambridge University Press (1990).
- [5] M. Crouch, 20th ICRC, Moscow, HE 4.1-2 (1987); E.V. Bugaev, Phys. Rev. **D58** (1998) 054001; Y.M. Andreyev, V.I. Gurentsov and I.M. Kogai, 20th ICRC, Moscow, HE 4.1-19,

- (1987); P.H. Barrett et al., Rev. Mod. Phys. 24 (1952) 133; L. M.Bollinger, Phys. Rev. 79 (1950) 207A; M. Aglietta et al., Nucl. Phys. B (Proc. Suppl.) 14B (1990) 193.
- [6] M. Aglietta et al, Phys. Rev. **D58** (1998) 092005.
- [7] M. Ambrosio et al., Phys. Rev. **D52** (1995) 3793.
- [8] A. Ferrari, T. Rancati and P.R. Sala, Proc. 3rd workshop on “Simulating Accelerator Radiation Environment”, SARE-3, KEK-Tsukuba, May 7–9 1997, H. Hirayama ed., KEK report Proceedings 97-5, p. 165 (1997)
- [9] A. Fassó et al., “Electron-photon transport in FLUKA: status” and “FLUKA: Status and Perspectives for Hadronic Applications”, in Proc. of MC2000 (Lisbon, Oct 2000). See also <http://www.cern.ch/fluka>.
- [10] Yu. D. Kotov and V. M. Logunov, 11th ICRC, Budapest, MU-50 (1969).
- [11] F. Arneodo *et al.*, ICARUS Collab., ICARUS-TM/2000-06, submitted to Elsevier Preprint.
- [12] M. Ambrosio et al., Phys. Rev. **D56** (1997) 1407; M. Ambrosio et al., Phys. Rev. **D56** (1997) 1418;
- [13] F. Arneodo *et al.* [ICARUS and NOE Collab.], “ICANOE: Imaging and calorimetric neutrino oscillation experiment,” LNGS-P21/99, INFN/AE-99-17, CERN/SPSC 99-25, SPSC/P314; see also A. Rubbia [ICARUS collaboration], hep-ex/0001052. Updated information can be found at <http://pcnometh4.cern.ch>.
- [14] S. Fukuda *et al.* [Super-Kamiokande Collaboration], Phys. Rev. Lett. **85**, 3999 (2000) [hep-ex/0009001].
- [15] M. Ambrosio et al., Phys. Lett. **B434** (1998) 451.
- [16] Y. Fukuda et al., Phys. Rev. Lett. **82** (1999) 2644.
- [17] P. Lipari and M. Lusignoli, Phys. Rev. D **58** (1998) 073005 [hep-ph/9803440].
- [18] ICARUS Collaboration, The ICARUS 50 l LAr TPC in the CERN  $\nu$  Beam, *Proceedings of 36th Workshop On New Detectors, Erice, Italy / 1-7 Nov. 1997*, World Scientific (1999) 3.
- [19] F. Arneodo et al. (ICARUS Collab.) Nucl.Instrum. Meth. **A449** (2000) 42.
- [20] C.Caso et al., “Review of particle physics”, **Eur. Phys. J. C 15** (2000).
- [21] V. Agrawal et al., Phys. Rev. **D53** (1996) 1314.
- [22] M. Ambrosio et al., Astroparticle Physics **9**(1998) 105.
- [23] ICARUS Collaboration, Study of solar neutrinos with the 600 t liquid argon ICARUS detector, *Nucl. Instr. and Methods* **A455** (2000) 376.
- [24] W. E. Ormand, P. M. Pizzochero, P. F. Bortignon and R. A. Broglia, Phys. Lett. B **345** (1995) 343 [nucl-th/9405007].
- [25] J. N. Bahcall, S. Basu and M. H. Pinsonneault, Phys. Lett. B **433** (1998) 1 [astro-ph/9805135].

- [26] J.N. Bahcall, Neutrino Astrophysics, Cambridge University Press (1989).
- [27] W. Trinder *et al.*, *Phys. Lett.* **B415** (1997) 211.
- [28] W. Liu *et al.*, *Z. Phys.* **A359** (1997) 1.
- [29] ICARUS Collaboration, On atmospheric  $^{39}\text{Ar}$  and  $^{42}\text{Ar}$  abundance, *Nucl. Instr. and Methods* **A356** (1994) 256.
- [30] V.D. Ashitkov *et al.*, *Nucl.Phys. Proc.Suppl.* **70** (1999) 233.
- [31] A. Somigliana, Misure di contaminazioni radioattive bassissime in materiali per schermature con particolare riferimento a piombo antico e moderno, Degree thesis, Università degli Studi di Milano (1989/90) in Italian.
- [32] F. Arneodo *et al.*, Neutron background measurements in the ICARUS area at the underground Gran Sasso Laboratory, *Il Nuovo Cimento* **A8** (1999) 819.
- [33] A. Esposito, Misure di radioattività nei campioni di materiale da utilizzare per strutture interne del LNGS dell'INFN, *LNF Report* **LNF-86/60** (1986) in Italian.
- [34] J.N. Bahcall *et al.*, *Phys. Lett. B* 477 (2000) 401, J.N. Bahcall *et al.*, *Phys. Rev. D* 62 (2000) 9304.
- [35] M. Shiozawa (Super-Kamiokande Collaboration), *ICHEP 2000 - XXXth Int. Conf. on HEP, Osaka, Japan, July 27-Aug 2, 2000*; Proceed. submitted to **World Scientific**  
K.S. Ganezer (Super-Kamiokande Collaboration), *DPF 2000 - Meeting of the Division of Particles and Fields of the APS, August 9-12, 2000 Columbus, Ohio, USA*; Proceed. submitted to **Int. Journal of Modern Physics A**
- [36] C. K. Jung, Feasibility of a next generation underground water Cherenkov detector: UNO, NNN99 at Stony Brook, hep-ex/0005046.
- [37] A. Bueno *et al.*, Nucleon Decay studies in a large Liquid Argon detector, NNN99 at Stony Brook, AIP Conference Proceedings Vol.533 (2000).
- [38] K.S. Babu, J.C. Pati and F. Wilczek, *Nucl. Phys.* **B566** (2000) 33 and hep-ph/9812538.
- [39] R. Dermisek, A. Mafi and S. Raby, hep-ph/0007213.
- [40] K. Hirata *et al.*, *Phys. Rev.* **D38** (1988) 448; *Phys. Rev. Lett.* **58** (1987) 1490.
- [41] R. Bionta *et al.*, *Phys. Rev. Lett.* **58** (1987) 1494.
- [42] A. Burrows, D. Klein, and R. Gandhi, *Phys. Rev.* D45 (1992) 3361.
- [43] A. Burrows, *Ann. Rev. Nucl. Part. Sci.* 40 (1990) 181.
- [44] R. Mayle, J. R. Wilson, and D. N. Schramm, *Ap. J.* 318 (1987) 288.
- [45] S. Woosley, J. Wilson, and R. Mayle, *Ap. J.* 302 (1986) 19.
- [46] H. A. Bethe, *Rev. Mod. Phys.* 62 (1990) 801.
- [47] K. Langanke, P. Vogel and E. Kolbe, *Phys. Rev. Lett.* **76** (1996) 2629 [nucl-th/9511032].
- [48] J. N. Bahcall and R. M. Soneira, *Ap. J. Supp.* 44 (1980) 73.
- [49] R. S. Raghavan, *Phys. Rev. D* **34** (1986) 2088.